Reliability Engineering and System Safety 267 (2026) 111836

Contents lists available at ScienceDirect

Reliability Engineering and System Safety

journal homepage: www.elsevier.com/locate/ress

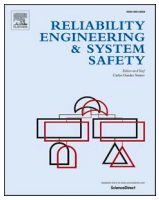

Markov process-based real-time risk forecasting for transmission towers during tropical cyclones to support grid resilience

Xinghong Chen [a], You Wu [a], Zhenguo Wang [c], Binbin Li [a,b], Naiyu Wang [a,*]

[a] College of Civil Engineering and Architecture, Zhejiang University, Hangzhou 310058, China
[b] ZJU-UIUC Institute, Zhejiang University, Haining 314400, China
[c] State Grid Zhejiang Electric Power Co., Ltd. Electric Power Science Research Institute, Hangzhou 310022, China

ARTICLE INFO

Keywords:
Transmission tower-line systems
Tropical cyclones
Wind fragility model
Markov Process
Progressive Structural Degradation
Risk forecasting
Infrastructure Resilience

ABSTRACT

Transmission towers are critical yet vulnerable components of power infrastructure, particularly under the sustained and fluctuating wind loads imposed by tropical cyclones (TCs). Traditional fragility-based risk models assess collapse using static, binary criteria, overlooking the progressive nature of structural degradation during multi-day TC events. This study proposes a Markov Process-based Risk Forecasting (MPRF) framework that dynamically captures cumulative damage of transmission towers under evolving wind conditions. Tower capacity is modeled as a discrete-state Markov chain with probabilistic transitions among intact, direction-specific damage, and collapse states. Conditional transition probability functions (CTPFs), pre-computed via pushover and nonlinear time-history simulations of tower-line system across a range of wind speeds and attack angles, populate the transition probability matrix (TPM) of the MPRF, enabling real-time state probability propagation driven by meteorological forecasts. Applied to Typhoon Lekima (2019) in Zhejiang Province, China, the MPRF identifies high-risk towers and lines earlier and more accurately than conventional binary models, emphasizing the importance of capturing damage accumulation. Results show that neglecting progressive deterioration can underestimate collapse risk by up to 30% and obscure near-collapse conditions. Comparison with post-event observations further demonstrates that MPRF captures a broader spectrum of system degradation, providing a more faithful representation of real-world impacts. By enabling adaptive and spatially explicit risk forecasts, MPRF provides an operationally scalable tool for proactive resilience planning and decision-making under evolving TC events.

1. Introduction

Power transmission networks are increasingly exposed to tropical cyclones (TCs), whose extreme winds pose serious threats to transmission towers. Climate-driven increases in TC frequency and intensity are escalating risks to power grid infrastructure [1]. Although reliability-based design have aimed to optimize the trade-off between structural efficiency and wind resistance [2,3], transmission towers remain particularly vulnerable to wind-induced failures, which often lead to widespread outages and limited mitigation options during TC events [4,5]. These growing challenges underscore the need for more advanced risk assessment frameworks to inform grid resilience enhancement and emergency response planning under TC conditions.

Fragility modeling remains the prevailing approach for quantifying tower vulnerability under extreme winds. By relating hazard intensities to the likelihood of exceeding defined failure thresholds, fragility curves serve as core tools in reliability engineering and risk analysis, including applications such as FEMA's HAZUS methodology [6]. Many studies estimate collapse probabilities using simplified structural analyses such as static pushover or limited-duration dynamic simulations [7]. Subsequent work has advanced the realism of these models by incorporating tower-line interactions to better capture system-level coupling effects [8–10], and by extending their scope to multi-hazard fragility assessments—such as those considering wind–earthquake interactions [11] and compound wind–rain scenarios [12,13]. Most existing fragility models for transmission towers adopt a binary-state formulation that assess only whether a tower remains intact or collapse. While these models yield valuable insights into collapse risk, they fundamentally overlook the progressive damage accumulation that typically precedes collapse failure, thereby limiting their ability to support real-time risk

* Corresponding author.
E-mail address: naiyuwang@zju.edu.cn (N. Wang).

https://doi.org/10.1016/j.ress.2025.111836
Received 8 July 2025; Received in revised form 12 September 2025; Accepted 24 October 2025
Available online 25 October 2025

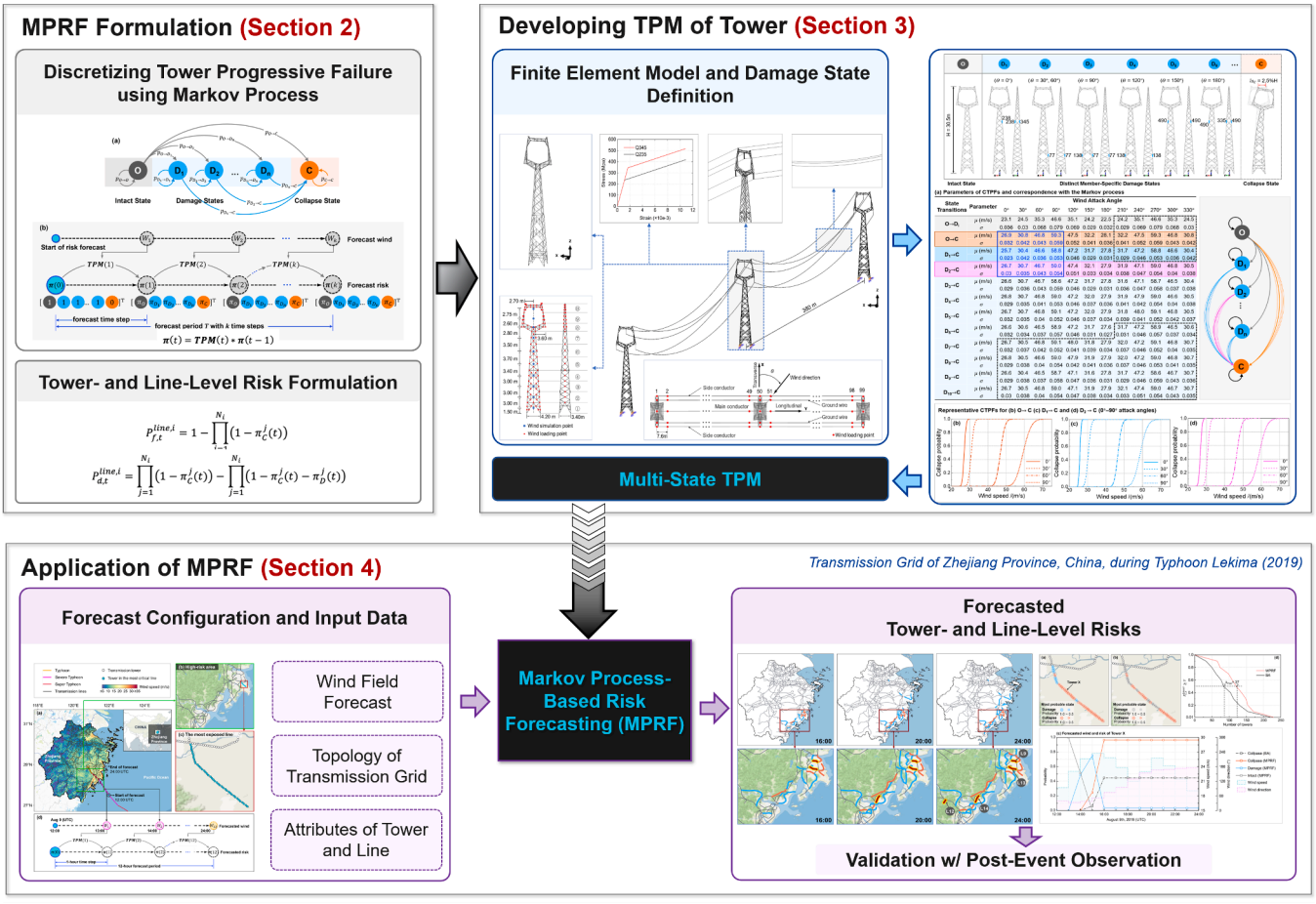

Fig. 1. Flowchart of MPRF framework development and its real-time application to risk forecasting of regional transmission systems.

forecasting continuously throughout evolving TCs.

Unlike sudden-onset hazards such as earthquakes, the predictable track and multi-day duration of TCs create a valuable window for proactive risk mitigation. This multi-day lead time allows grid operators to identify emerging vulnerabilities, pre-position crews, and implement targeted interventions to prevent cascading outages. However, to fully leverage this window, risk assessment frameworks must advance beyond the conventional binary fragility models to capture how tower condition evolves dynamically under sustained TC wind exposure.

Extensive evidence from full-scale experiments [14], numerical simulations [15,16], and post-disaster damage records [17] consistently indicates that transmission towers undergo sequential deterioration—typically progressing from minor buckling and connection loosening to bracing failures and, eventually, collapse. Recent studies further suggest that even prolonged yet moderate monsoon loading can initiate damage, gradually weakening structural integrity by exposing vulnerable members to cumulative fatigue [18–20]. Nevertheless, under the more intense and sustained TC winds, the progressive damage that accumulates during such sequential deterioration—which significantly heightens tower susceptibility to failure—remains insufficiently explored in existing structural performance evaluations. Neglecting these cumulative effects compromises the accuracy of system-level risk projections and weakens preemptive mitigation strategies during TC events.

Recent advancements have begun integrating real-time wind forecasts with power system risk predictions. For example, Xue et al. [10] applied a dynamic simulation framework to evaluate the performance of a synthetic transmission system during Hurricane Harvey, while Cai et al. [21] employed a Kriging-based approach to estimate time-dependent failure probability of transmission lines during Typhoon Mujigea. Sang et al. [22] further incorporated fragility-informed collapse probabilities into day-ahead optimization models for grid risk mitigation. Beyond the power grid, Mühlhofer et al. [23] extended a fragility-based risk framework to evaluate cascading service disruptions during Hurricane Michael. Building on these efforts, recent studies have improved the spatial and temporal fidelity in grid risk predictions by advancing both structural and hazard modeling. On the structural side, new methods have been proposed to capture correlations across tower networks [24–26] and to probabilistically quantify cascading tower failures under compound failure scenarios [27]. In parallel, wind field representations have been enhanced through microscale (~100 m) dynamic and probabilistic downscaling tailored to grids in complex terrain [28,29], as well as through deep learning–based assimilation of multi-source, real-time data to reconstruct high-resolution wind fields for power systems [30].

Despite these advances, nearly all these frameworks continue to rely on binary fragility curves evaluated at each forecast interval, implicitly assuming that towers "reset" to their full capacity after each interval and overlooking the cumulative nature of damage under sustained TC winds. Du and Hajjar [31] took a notable step by utilizing incremental dynamic analyses over complete hurricane wind histories, accounting for the accumulation of nonlinear and dynamic effects. More recently, Du et al. [32] emphasized the role of progressive collapse in transmission tower-line systems, demonstrating its impact on shifting fragility functions and degrading overall system reliability. However, both studies stopped short of embedding these degradation dynamics into a continuously updating, operational risk prediction model. Meanwhile, other researchers have proposed multi-state fragility models that categorize

tower limit states into discrete levels—slight, moderate, extensive damage, and collapse—based on different structural response criteria. These include performance-based thresholds [1], distinct failure modes [33], and orientation-dependent top displacement metrics [34]. While these models enhance vulnerability representations, most remain static in nature—mapping each damage state to a fixed wind intensity and, most importantly, assuming that transitions occur as direct one-step jumps from "intact" to each damage or collapse state. As a result, they are unable to capture the gradual degradation of structural capacity under sustained wind exposure, nor can they support hour-by-hour risk forecasting during an evolving TC.

Bridging this gap requires a new modeling paradigm that explicitly and continuously tracks cumulative damage progression throughout the lifecycle of a TC event—enabling real-time, temporally adaptive grid risk forecasting that better supports proactive resilience strategies. To address this need, we propose a **Markov Process-based Risk Forecasting (MPRF)** framework that extends traditional fragility modeling into the temporal domain. By conceptualizing tower degradation as a discrete-state Markov process, where state transitions (between intact, intermediate damage, and collapse) are governed by the evolving wind field, the **MPRF** continuously and explicitly tracks cumulative damage of towers as TCs progress. This approach is both physically grounded and operationally scalable, yielding a continuous, state-dependent forecast of grid vulnerability. Key contributions include:

- **Progressive multi-state modeling**: Tower capacity deterioration is modeled as a discrete-state Markov process with transitions across multiple states, capturing gradual failure beyond binary models.
- **Computationally tractable formulation**: Transition probabilities are informed by comprehensive structural dynamic response simulations but implemented in a simplified Markov framework, enabling real-time, region-wide risk forecasting.
- **Dynamic, forecast-driven risk propagation**: Real-time wind forecasts are assimilated through a time-dependent transition matrix, allowing tower specific state probabilities to evolve dynamically with forecasted changing TC condition.
- **Enhanced real-time support for grid resilience**: Application to Typhoon Lekima demonstrates the MPRF's ability to capture cumulative damage and identify high-risk towers earlier than conventional models, supporting targeted maintenance and emergency planning.

Together, these advances enable a truly dynamic, temporally adaptive risk-forecasting tool that can guide proactive resilience measures and emergency planning throughout the lifecycle of a TC event. The remainder of this paper is structured as follows: Section 2 describes the development of the MPRF framework; Section 3 details its implementation for a representative transmission tower; and Section 4 presents a comparative evaluation against traditional fragility models in the context of a real-world TC event. The flowchart of the MPRF framework development and its real-time application is shown in Fig. 1.

2. Formulation of a Markov process-based risk forecast framework for transmission towers and lines

2.1. Probabilistic modeling of transmission tower collapse under TC winds

Assessing the collapse probability of a transmission tower subjected to strong and sustained winds during TC event is a fundamental task in forecasting power grid risk. The collapse probability, P_C, is defined as the probability that the tower resistance R is exceeded by the total wind load W:

$$\begin{aligned} P_C &= P(R < W) = P\left(R < W_m + W_f\right) \\ &= w_m \in W_m \int P\left(R < w_m + W_f\right) \cdot f_{W_m}(w_m) \cdot dw_m \\ &= w_m \in W_m \int P_{C,R|w_m} \cdot f_{W_m}(w_m) \cdot dw_m \end{aligned} \tag{1}$$

where W_m denotes the steady (mean) wind component, based on time-averaged wind speed and direction, while W_f represents the zero-mean fluctuating component. The function $f_{w_m}(w_m)$ is the probability density function of the mean wind speed W_m. The conditional probability $P_{C,R|w_m}$ denotes the likelihood of collapse given a specific mean wind intensity w_m, and corresponds to the widely adopted fragility function. The uncertainty in W_f is not explicitly integrated in Eq. (1); instead, it is embedded within $P_{C,R|w_m}$ through probabilistic dynamic simulations in which turbulent wind is modeled as a stationary Gaussian processes using spectral methods (e.g., Davenport, or Kaimal spectra; [35]). In principle, uncertainty in R, stemming from material properties and geometric variability, should also be considered. However, in this study, R is treated deterministically, based on the rationale that wind-induced uncertainty is more dominant [36]. The influence of wind uncertainty propagates into tower state probability via cumulative damage over time, as further detailed in Section 2.2.

However, in reality tower failure under sustained TC winds is neither instantaneous nor binary, but unfolds through a sequence of damage accumulation under a sequence of changing wind. As wind-induced lateral forces increase, individual leg members first experience local buckling, which reduces their stiffness and redistributes loads to neighboring elements. This in turn can overload diagonal bracings—originally designed for tension—causing secondary buckling and further capacity loss. As more members yield, stress concentrations migrate through the lattice until plastic hinges form, precipitating global collapse.

To capture this cascade of damage, we represent tower resistance not as a single static value but as a time-indexed sequence, $\{R_1, R_2, \ldots, R_t\}$, where R_t denotes the remaining load capacity after cumulative wind exposure up to time step t. Likewise, wind forcing projected by operational weather forecast also evolves temporally during a TC event, and is represented as a sequence $\{W_1, W_2, \ldots, W_t\}$, where W_t includes wind speed V_t and attack angle Θ_t. The probability that the tower has not collapsed by time t is the joint survival probability:

$$P(R_1 \geq W_1, R_2 \geq W_2, \ldots, R_t \geq W_t) \tag{2}$$

so, the cumulative collapse probability is simplified as:

$$P_{C,t} = 1 - P\left(\bigcap_{i=1}^{t} \{R_i \geq W_i\}\right) \tag{3}$$

Thus, Eq. (3) couples the evolving external wind loads $\{W_t\}$ with the internal resistance sequence $\{R_t\}$, yielding a full probabilistic, time-resolved forecast of tower collapse under TC conditions.

2.2. Discretizing progressive failure using a discrete-state Markov process

Running a high-fidelity nonlinear analysis to obtain $P_{C,t}$ at every forecast time step in real time during an approaching TC is impractical: the member-level interactions are highly nonlinear and tower risk predictions must be updated frequently. To keep the problem tractable, we coarse-grain the tower's condition into three mutually exclusive states:

- **Intact state** (s_O): The tower behaves purely elastically, with no permanent damage and full load-carrying capacity.
- **Damage state** (s_D): Triggered when tower response metric (e.g., tower-top displacement) first exceeds the damage limit state threshold ls_D. This indicates the onset of localized inelastic behavior—such as member buckling or yielding—reducing overall stiffness

and capacity while preserving global structural integrity. As an early warning, s_D signals compromised performance prior to collapse.

- **Collapse state** (s_C): Triggered when tower response metric surpasses the collapse limit state threshold ls_C. This threshold corresponds to large deformations, disrupted load paths, and functional failure (for example, conductor misalignment), marking complete structural collapse and service interruption.

By mapping continuous degradation—elastic → localized damage → global collapse—onto these three states, we preserve the progression of failure while avoiding the computational burden of tracking myriad subtle modes. Applying only two thresholds (ls_D and ls_C) makes it straightforward to assign each tower to its current state and, in turn, to update state probabilities via a fast, Markov-based transition model at each time step. This abstraction balances physical fidelity with operational speed, enabling real-time risk forecasts as a TC unfolds. (The refinement of the framework to incorporate multiple damage scenarios, where finer resolution is required, is presented later in this section.)

At any time step t, the tower's state is represented by a variable $S_t \in \{s_O, s_D, s_C\}$, corresponding to intact, damage, or collapse state. Owing to inherent uncertainties in wind loading and structural variability, the tower's states are modeled probabilistically and described by the state probability vector:

$$\boldsymbol{\pi}(t) = [\pi_O(t),\ \pi_D(t),\ \pi_C(t)]^{\mathrm{T}},\quad \sum_{i\in\{O,\ D,\ C\}} \pi_i(t) = 1 \tag{4}$$

where $\pi_i(t) = P[S_t = s_i]$; specifically, $\pi_C(t)$=$P_{C,t}$ in Eq. (3).

We model the evolution of $\boldsymbol{\pi}(t)$ as a discrete-time Markov chain. Because capacity degradation is monotone (a tower cannot "heal" by itself once damaged) and wind fluctuations become statistically independent over minute-long intervals, the state at time t depends only on the state at $t-1$ and the current wind load W_t. Denoting the time-dependent transition probability matrix by $\boldsymbol{TPM}(t)$, we have:

$$\boldsymbol{\pi}(t) = \boldsymbol{TPM}(t) * \boldsymbol{\pi}(t-1) \tag{5}$$

The irreversibility of the damage process implies a lower-triangular $\boldsymbol{TPM}(t)$:

$$\boldsymbol{TPM}(t) = \begin{bmatrix} p_{O\to O}(t) & 0 & 0 \\ p_{O\to D}(t) & p_{D\to D}(t) & 0 \\ p_{O\to C}(t) & p_{D\to C}(t) & 1 \end{bmatrix} \tag{6}$$

with each column summing to unity.

Each entry $p_{i\to j}(t)$ is a **conditional transition-probability function (CTPF)**, representing the probability of transitioning to state s_j at time t, conditional on W_t at time t and the prior state s_i at $t-1$:

$$p_{i\to j}(t) = P\left(S_t = s_j \middle|\ S_{t-1} = s_i, W_t\right) \tag{7}$$

and is computed via exceedance-based fragility logic. Let d_t be the selected tower response metric (e.g., tower-top displacement) under wind conditions $W_t = (V_t, \Theta_t)$ at time t, then:

- Collapse from intact:

$$p_{O\to C}(t) = P(d_t > ls_C | S_{t-1} = s_O, W_t) \tag{8}$$

- Collapse from damage:

$$p_{D\to C}(t) = P(d_t > ls_C | S_{t-1} = s_D, W_t) \tag{9}$$

- Damage from intact:

$$\begin{aligned} p_{O\to D}(t) &= P(ls_C \geq d_t > ls_D | S_{t-1} = s_O, W_t) \\ &= P(d_t > ls_D \middle|\ S_{t-1} = s_O, W_t) - p_{O\to C}(t) \end{aligned} \tag{10}$$

The remaining entries in the $\boldsymbol{TPM}(t)$ are computed by complementarity:

$$p_{D\to D}(t) = 1 - p_{D\to C}(t) \tag{11}$$

$$p_{O\to O}(t) = 1 - p_{O\to D}(t) - p_{O\to C}(t) \tag{12}$$

This fully defines the $\boldsymbol{TPM}(t)$ at each forecast time step, allowing forward propagation of $\boldsymbol{\pi}(t)$ and producing a time-resolved, probabilistic forecast of tower collapse under evolving wind loads.

In reality, wind from different directions engages distinct sets of tower members, activating specific failure mechanisms depending on the attack angle. To capture this, we refine the single "damage" state s_D into n direction-specific damage states. The state space is thus expanded to $\{s_O,\ s_{D_1},\ s_{D_2},\ \cdots,\ s_{D_n},\ s_C\}$, with the corresponding extended state probability vector:

$$\boldsymbol{\pi}(t) = [\pi_O(t),\ \pi_{D_1}(t), \pi_{D_2}(t), \ldots, \pi_{D_n}(t),\ \pi_C(t)]^{\mathrm{T}} \tag{13}$$

Each damage state s_{D_i} represents the onset of local buckling or yielding in a particular group of members—typically those carrying the highest loads when wind attacking from a particular angular sector $\mathscr{A}_i$ respective to the tower orientation.

Once a damage scenario s_{D_i} is initiated, the model assumes the structure cannot switch to another damage scenario s_{D_j} $(i \neq j)$; instead, further degradation proceeds along the same path until collapse. This "no-transition" assumption reflects two physical realities: (1) Path dependency of plastic deformation, where initial member buckling redistributes stiffness in a unique way that governs all subsequent behavior; and (2) Gradual wind-direction changes in TCs, which rarely reverse sufficiently to re-load previously undamaged members.

Mathematically, this yields a sparse, lower-block-triangular transition matrix $\boldsymbol{TPM}(t) \in \mathbb{R}^{(n+2)\ \times\ (n+2)}$, with all off-path transitions $p_{D_i\to D_j}(t)$ (for $i \neq j$) set to zero:

$$TPM(t) = \begin{bmatrix} p_{O\to O}(t) & 0 & 0 & \cdots & 0 & 0 \\ p_{O\to D_1}(t) & p_{D_1\to D_1}(t) & 0 & \cdots & 0 & 0 \\ p_{O\to D_2}(t) & 0 & p_{D_2\to D_2}(t) & \cdots & 0 & 0 \\ \vdots & \vdots & \vdots & \ddots & \vdots & \vdots \\ p_{O\to D_n}(t) & 0 & 0 & \cdots & p_{D_n\to D_n}(t) & 0 \\ p_{O\to C}(t) & p_{D_1\to C}(t) & p_{D_2\to C}(t) & \cdots & p_{D_n\to C}(t) & 1 \end{bmatrix} \tag{14}$$

Moreover, transitions from the intact state to a particular damage scenario occur only when the instantaneous wind attack angle Θ_t falls within the angular sector $\mathscr{A}_i$, which represents the group of wind directions that induce the same damage scenario; each Θ_t is associated with a direction-dependent onset threshold $ls_{D_i}^{(\Theta_t)}$; i.e.:

$$p_{O\to D_i}(t) = \begin{cases} 0, & \Theta_t \notin \mathscr{A}_i, \\ P\left(d_t > ls_{D_i}^{(\Theta_t)} \middle| S_{t-1} = s_O,\ W_t = (V_t, \Theta_t)\right) - p_{O\to C}(t), & \Theta_t \in \mathscr{A}_i. \end{cases} \tag{15}$$

The remaining CTPFs—including the intact-to-collapse $p_{O\to C}(t)$, the damage-to-collapse $p_{D_i\to C}(t)$, and their complementarity conditions—are defined exactly as in the three-state model. All CTPFs, together with the damage thresholds ls_D and the collapse threshold ls_C, are precomputed before the TC event using the detailed structural analyses described in Section 3.

By embedding these direction- and path-specific damage states within a Markov-chain framework, we obtain a probabilistic, time-evolving model that (a) respects the physical irreversibility of tower capacity degradation, (b) accounts for wind-direction effects on member load paths, and (c) remains computationally efficient for real-time risk forecasting during TC events. This extended ***TPM***, driven by forecasted wind speed and attack angle, thus underpins an operationally scalable tool for continuously updating collapse and damage probabilities across

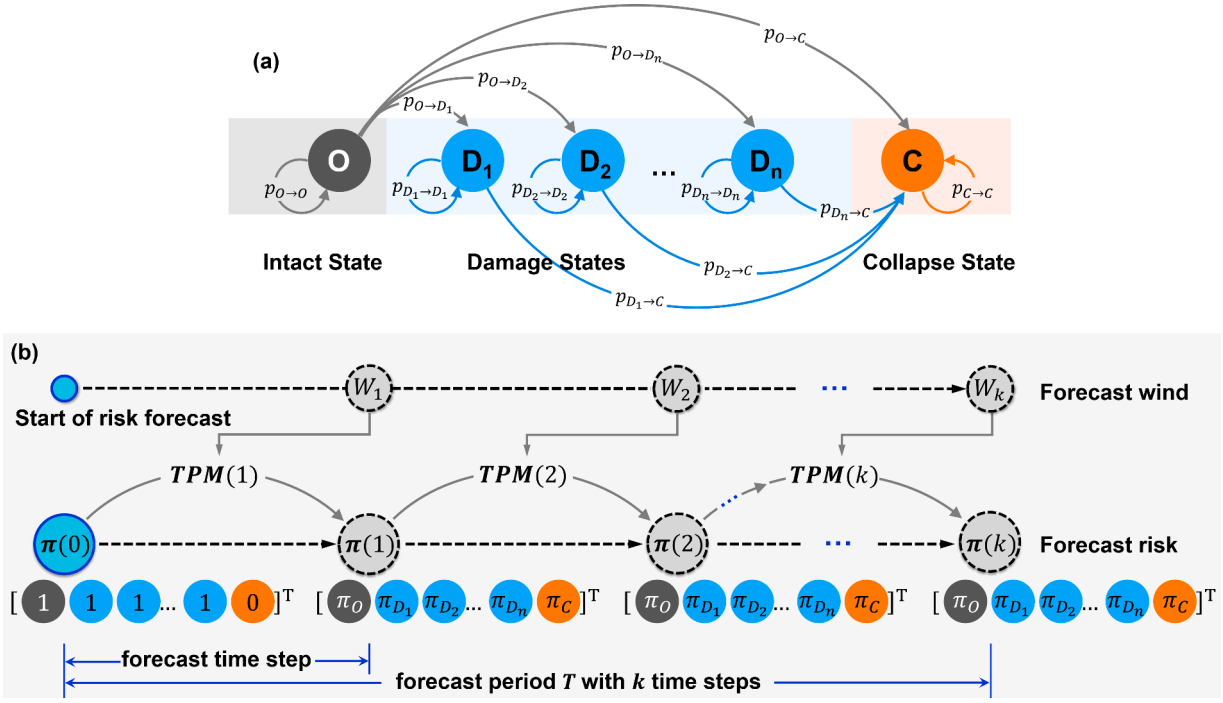

Fig. 2. (a) Discrete-state Markov chain representation of tower failure dynamics; (b) Recursive real-time risk forecasting using MPRF framework.

entire transmission networks under TC conditions.

2.3. Markov process-based risk forecasting (MPRF) for tower and line-level assessment

Building on the predefined discrete states and precomputed CTPFs introduced earlier, the MPRF model predicts the evolving vulnerability of transmission towers and lines in real time under forecasted wind conditions $W_t = (V_t, \Theta_t)$. The system evolves as a discrete-time Markov chain, as illustrated in Fig. 2.

At each forecast step t, the transition probability matrix $\boldsymbol{TPM}(t)$ is populated using the forecast wind speed V_t and attack angle Θ_t based on the corresponding CTPFs. Repeating this process over a forecast horizon T (comprising k steps) yields forward-looking, time-resolved risk forecast (Fig. 2(b)) for the grids.

The MPRF procedure consists of three key steps:

1. *TPM* Assembly:

For each forecast time step t, extract the forecast mean wind speed V_t and attack angle Θ_t from numerical meteorological forecasts W_t. Populate $\boldsymbol{TPM}(t)$ by evaluating:

$$p_{i\to j}(t) = P\left(S_t = s_j \middle| S_{t-1} = s_i, W_t\right)$$

for each state pair $s_i \to s_j$ using the corresponding precomputed and pre-embedded CTPFs.

2. State Propagation:

Initialize every tower in the intact state:

$$\boldsymbol{\pi}(0) = (1,\ 0,\ \ldots,\ 0)^{\mathrm{T}}$$

Then recursively update:

$$\boldsymbol{\pi}(t) = \boldsymbol{TPM}(t) * \boldsymbol{\pi}(t-1) = [\pi_O(t),\ \pi_{D_1}(t), \pi_{D_2}(t), \ldots, \pi_{D_n}(t),\ \pi_C(t)]^{\mathrm{T}}$$

of particular interest are the cumulative collapse probability $P_{C,t}$ and the damage probability $P_{D,t}$, for each tower at step t:

$$P_{C,t}^{tower} = \pi_C(t) \tag{16}$$

$$P_{D,t}^{tower} = \pi_D(t) = \sum_{i=1}^{n} \pi_{D_i}(t) \tag{17}$$

3. Line-Level Aggregation:

Each transmission line i is modeled as a series of N_i towers. For tractability, we adopt the commonly used assumption of independent tower failures—widely applied in engineering risk analysis [21,10]—to estimate line-level risk. This assumption yields a conservative upper bound on failure probability and ensures computational feasibility. More refined formulations, such as incorporating spatial correlations among towers [24] or cascading effects [27], could further improve line-level assessments; however, these extensions fall beyond the scope of the present study. Importantly, the choice of line-level aggregation strategy does not affect the validity of the proposed MPRF framework, which is fundamentally focused on modeling tower-level deterioration and state transitions under evolving TC winds.

Under this assumption, the line's failure and damage probabilities at time t are computed as:

$$P_{f,t}^{line,i} = 1 - \prod_{j=1}^{N_i} \left(1 - \pi_C^j(t)\right) \tag{18}$$

and its damage probability is:

$$P_{d,t}^{line,i} = \prod_{j=1}^{N_i} \left(1 - \pi_C^j(t)\right) - \prod_{j=1}^{N_i} \left(1 - \pi_C^j(t) - \pi_D^j(t)\right) \tag{19}$$

By repeating these three steps—$\boldsymbol{TPM}(t)$ assembly driven by latest wind forecast, recursive propagation of each tower's state vector, and aggregation to line-level probabilities—MPRF delivers a time-resolved, spatially explicit risk forecast. Updated in near real time with each incoming meteorological forecast, this framework lets operators identify which towers and lines are most likely to suffer damage or collapse,

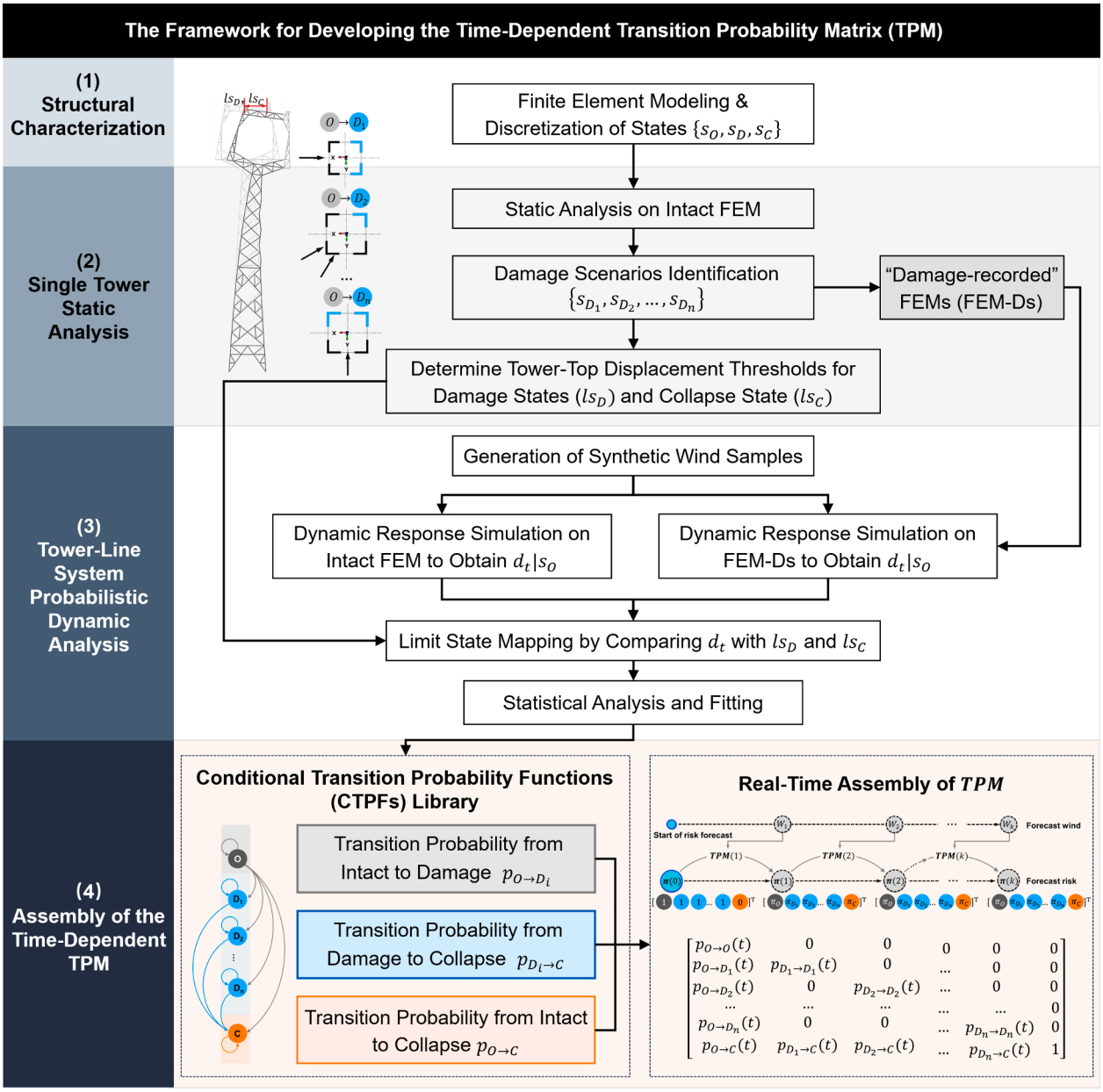

Fig. 3. Overall flowchart for developing the time-dependent TPM.

thereby guiding targeted inspections, resource prepositioning, and other resilience-enhancing actions during an evolving TC threat.

3. Developing transition probability matrix of tower

This section describes how we generate, ahead of any TCs, the CTPFs that pre-embedded in the ***TPM*** structure used by the MPRF framework in real time. A representative 2300ZM1 lattice transmission tower—commonly used in southeastern China's TC-prone coastal regions—is selected as the prototype structure. As illustrated in Fig. 3, the methodology consists of four sequential stages: (1) structural characterization through finite element modeling and discretization of states; (2) pushover analysis for damage onset and collapse capacity; (3) derivation of CTPFs via probabilistic nonlinear time-history simulations; and (4) assembly of the multi-state time-dependent ***TPM***.

3.1. Finite element model and discretization of states

The selected 2300ZM1 prototype is a 30.5-meter-tall coastal transmission tower (approximately 220 kV class), composed of equilateral angle-steel sections. The primary load-bearing members are made of high-strength Q345 steel, while the secondary bracing members use Q235 steel. The finite element model (FEM) was developed in ABAQUS [37] and is illustrated in Fig. 4(a). All structural members were modeled using Euler-Bernoulli beam elements (ABAQUS B31), comprising a total of 713 elements—124 for the main legs and 589 for bracing and secondary members. A bilinear isotropic hardening model was employed to characterize the steel behavior, capturing elastic-plastic deformation with strain hardening [38], as shown in Fig. 4(b). Bolted connections were idealized as rigid, consistent with the actual joint detailing in which gusset plates and multiple bolts on both flanges provide substantial rotational restraint and enable moment transfer—a simplification commonly employed in prior transmission tower studies [21,9,39]. The tower base was assumed to be fully fixed. To represent realistic

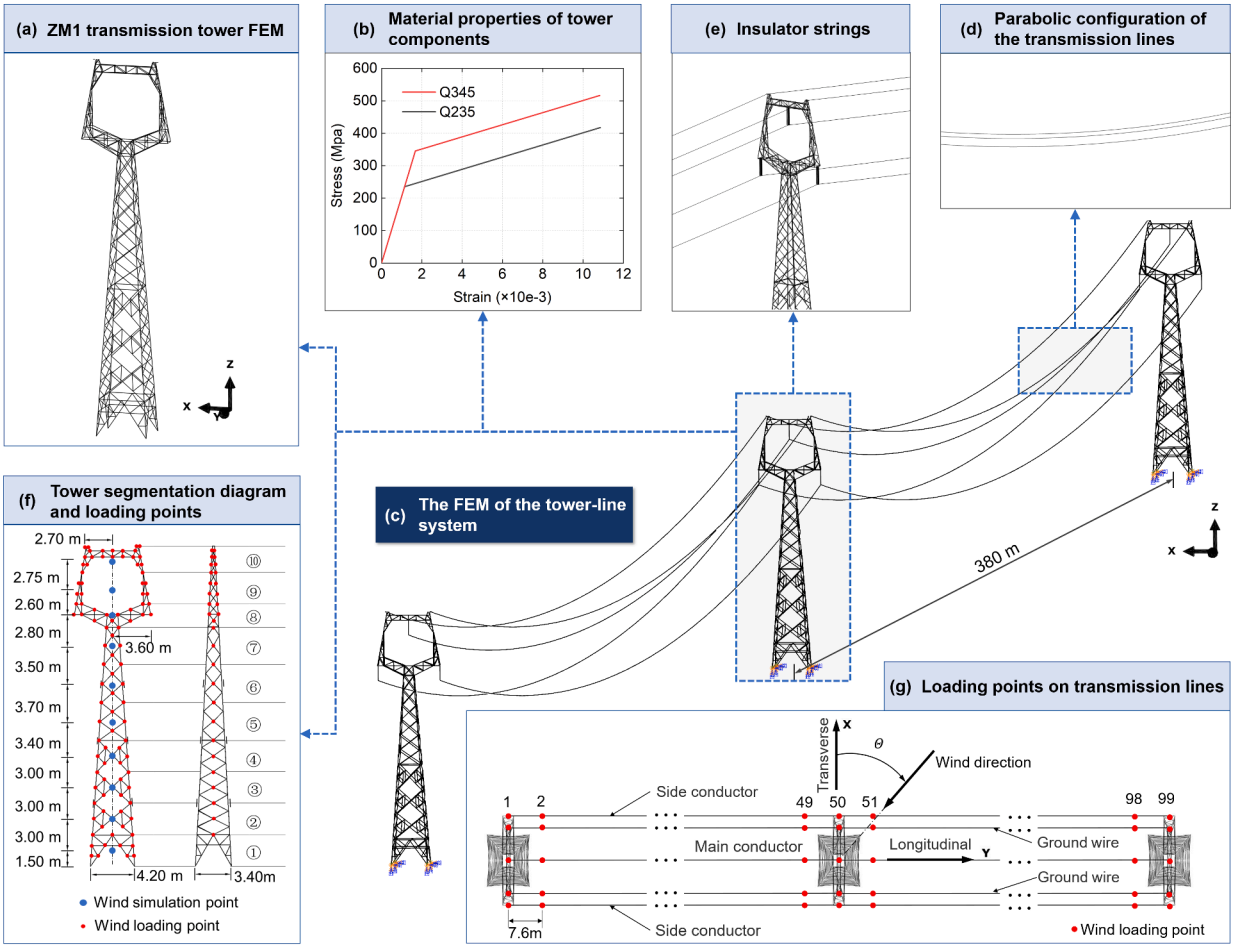

Fig. 4. Illustration of finite element models.

Table 1
Material properties of angle steel and transmission lines.

Member Parameters	Angle Steel		Conducting Wire	Ground Wire
	Q345	Q235	LGJ-400/35	JLB4-150
Yield Stress f_y(MPa)	345	235	–	–
Young's Modulus E (MPa)	2.06×10^5	2.06×10^5	6.50×10^4	1.09×10^5
Hardening Modulus E_{sh} (MPa)	$0.1E$	$0.1E$	–	–
Weight (N/m)	–	–	13.49	6.96
Diameter (mm)	–	–	27.00	15.80

structural imperfections resulting from fabrication and erection, initial geometric imperfection with 0.1% of the tower height was incorporated by imposing the first global buckling mode shape [33,40].

To realistically capture boundary conditions and wind-induced dynamic interactions, we embed the central prototype in a three-tower span (380 m spacing), with its two neighboring towers providing boundary support (Fig. 4(c)). Conductors are modeled as truss elements (ABAQUS T3D2) with pinned ends and a "no-compression" attribute to allow slackening. The initial sag of the conductors is established by an iterative tensioning procedure [41,42], resulting in the catenary shape shown in Fig. 4(d). Insulator strings, whose stiffness far exceeds that of towers and conductors, are likewise represented by high-stiffness truss elements with pinned ends (Fig. 4(e)). Finally, Rayleigh damping is implemented with a damping ratio of 1% for the tower and 2% for the transmission lines [43]. A summary of the material and geometric properties for all components is provided in Table 1.

We define our two response thresholds ls_D and ls_C—and hence the three discrete tower states $\{s_O, s_D, s_C\}$—using established structural-engineering criteria. **The damage state s_D threshold** is taken as the first violation of the axial-stability criterion in any primary member, per the Chinese steel-structure code [44]:

$$\frac{N}{\varphi A f} \leq 1.0 \tag{20}$$

where N is the member's axial force, A is its cross-sectional area, f is the design strength, and φ is the slenderness-dependent stability coefficient. Exceeding this limit indicates local buckling—a well-documented, wind-induced failure mode in lattice towers [14]—which triggers a loss of stiffness and redistribution of internal forces while the structure as a whole remains stable [1]. The corresponding tower-top displacement at that instant is our damage threshold, ls_D.

The collapse state s_C threshold is defined as the tower-top displacement beyond which the tower can no longer fulfil its essential functions—such as maintaining conductor clearance or geometric stability. After comparing common collapse indicators—fixed-height-ratio [22], first buckling-point displacement [7], and ultimate displacement [33]—we adopt the fixed-height-ratio from pushover analysis for its balance of mechanical fidelity and simplicity. This single collapse threshold, ls_C, applies equally to intact and pre-damaged configurations when computing conditional transition probabilities $p_{O\to C}$ and $p_{D\to C}$ within the CTPF framework.

Together, these two displacement thresholds—ls_D and ls_C—establish a clear, code-based discretization of tower behavior into intact, damage,

(a) Damage scenarios under symmetric wind attack angles based on pushover analysis

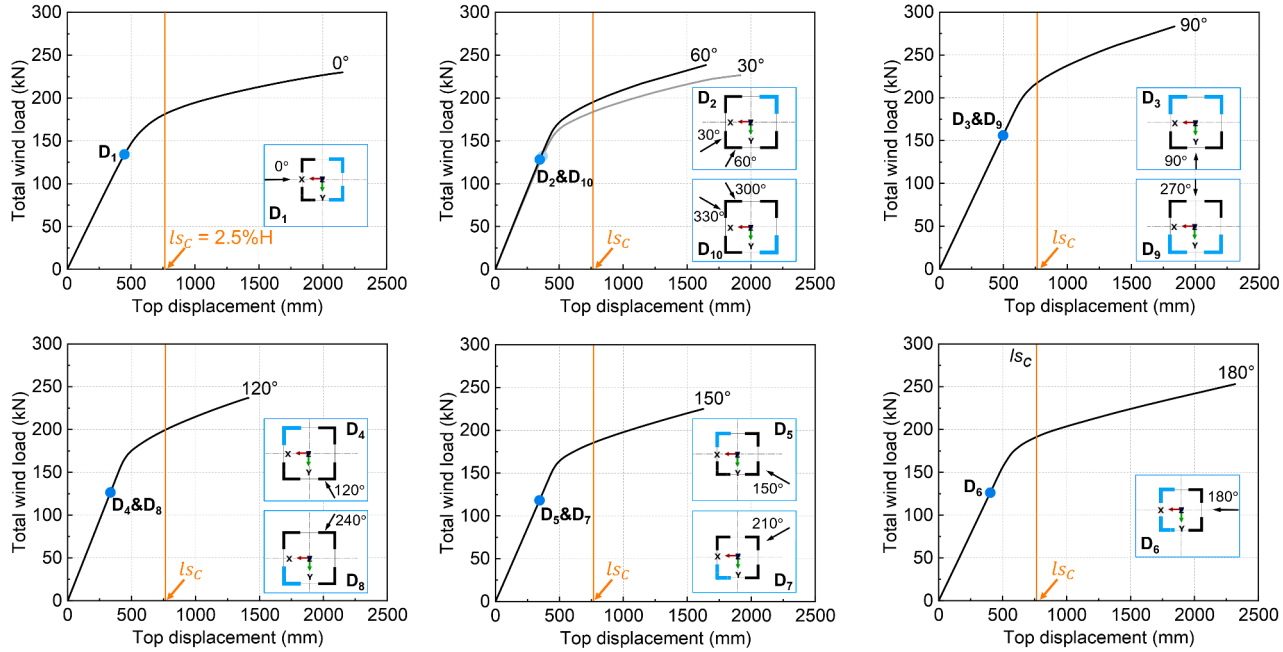

(b) Tower-top displacements and buckling Member IDs for damage scenarios

	D_1	D_2	D_3	D_4	D_5	D_6	D_7	D_8	D_9	D_{10}
Tower-Top Disp ls_{D_i} (mm)	448	370, 348	497	335	344	403	344	335	497	370, 348
1st buckling Member ID	345, 238	77	77, 138	138	490	490, 335	335	313	79, 313	79
2nd buckling Member ID	492, 342	88	88, 186	186	138	511, 368	313	306	79, 313	91

(c) Schematic of discrete structural states used for CTPF derivation

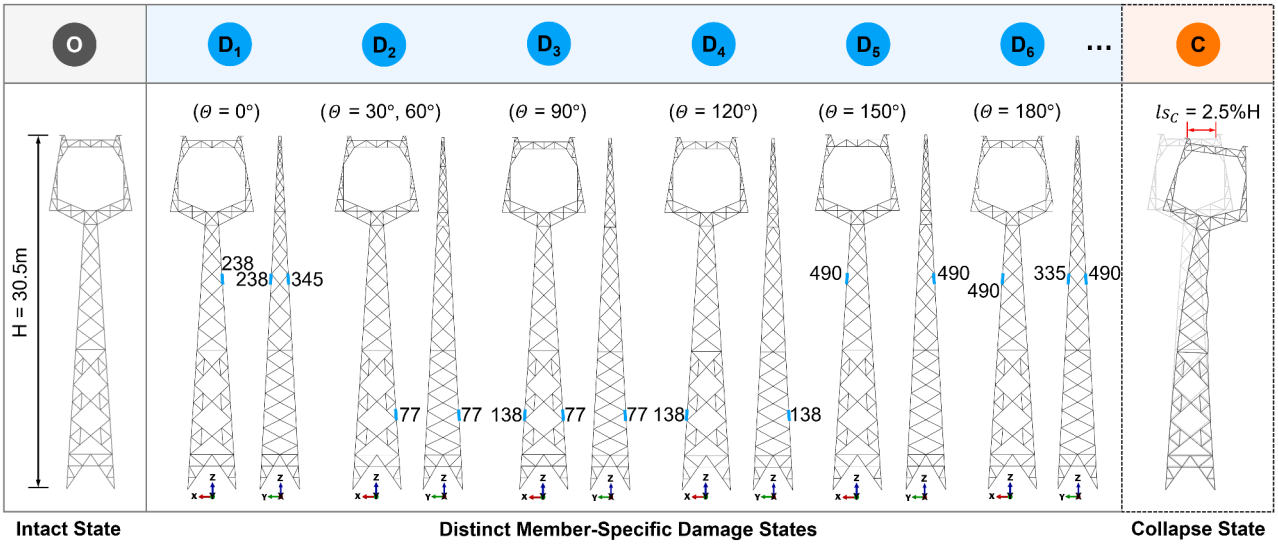

Fig. 5. (a) Damage scenarios under symmetric wind attack angles based on pushover analysis; (b) Tower-top displacements and buckling Member IDs for each of damage scenarios; (c) Schematic of discrete structural states used for CTPF derivation.

and collapse states, forming the foundation for the Markov-based ***TPM*** developed in Section 2.

3.2. Static analysis for damage onset and collapse capacity

Nonlinear static (pushover) analyses were conducted on the *intact* FEM (Section 3.1) to identify (i) Damage onset threshold (ls_D): the lateral tower-top displacement at which the first primary member buckles; and

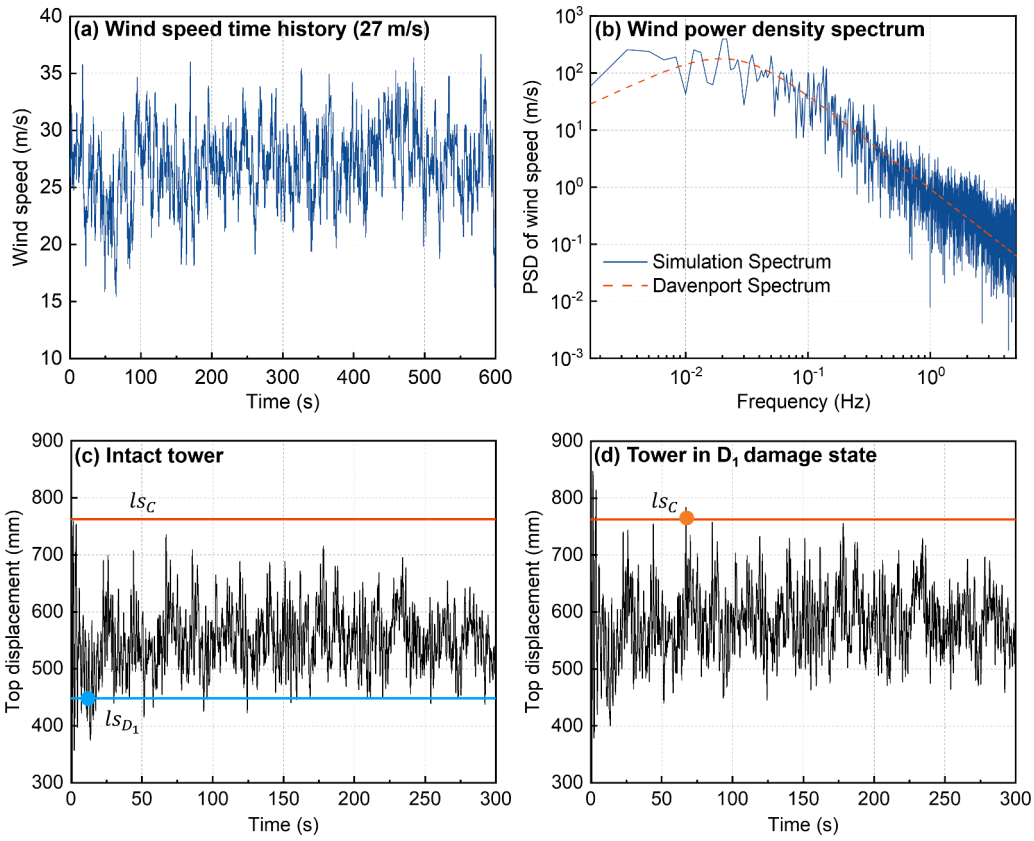

Fig. 6. Simulated sample of (a) wind speed time history and (b) wind power spectrum density spectrum for 10-minute mean wind speed of 27 m/s at 10m above ground; Corresponding dynamic responses of (c) intact tower and (d) tower in D_1 damage state.

(ii) Collapse capacity threshold (ls_C): the tower-top displacement at which the tower reaches its global instability limit state.

Static wind forces from the two adjacent spans were first converted into equivalent nodal loads at the conductor attachment points [45].To account for the vertical variation of wind pressure, the tower shaft was partitioned into ten equal segments; the height-dependent pressures, derived from the 10 m reference speed V_{10} and the vertical profile (DLT 5154-2012 [46], hereafter "the technical code"), were then lumped at the corresponding segment nodes (Fig. 4(f)).

In a TC event, wind attack angles can vary substantially over time, necessitating full-circle directional coverage. Given the directional dependence of lattice tower damage and failure, wind attack angles Θ were discretized into 12 directions (0°, 30°, …, 330°), where each angle represents the clockwise direction from the tower's transverse axis (see Fig. 4(g)). A 30° resolution balances directional sensitivity with computational feasibility [9], and forecasted wind directions are treated as their nearest discrete direction (e.g., –15° to +15° are evaluated as 0°).

Based on this, pushover analyses were performed for wind attack angles of 0°, 30°, ..., 180° to identify distinct damage scenarios. Other directions are structurally equivalent due to symmetry about the transverse axis. For each wind attack angle Θ, the corresponding tower-top displacement at local buckling onset was recorded as the direction-specific damage threshold $ls_{D_i}^{(\Theta)}$. Fig. 5(a) provides an overview of the identified scenarios. Based on the initial buckling pattern, wind attack angles inducing the same set of buckled members were grouped into a damage scenario D_i. For instance, wind attack angles of 30° and 60° both trigger buckling in member 77 (followed by 88) and are grouped into scenario D_2, with associated thresholds $\left\{ls_{D_2}^{(30)},\ ls_{D_2}^{(60)}\right\}$, and likewise for wind attack angles of 300° and 330°. In total, ten damage scenarios (D_1, $D_2, \cdots,\ D_{10}$) were defined, spanning all wind directions to account for TC-induced variability, each with a specific buckling pattern and tower-top displacement thresholds, as summarized in Fig. 5(b).

Notably, beyond the initial damage, increasing wind loads did not trigger transitions between distinct damage scenarios, as reflected by the subsequent buckling members recorded in Fig. 5(b) for each wind attack angle. Instead, each set of initial buckled members established a unique redistribution of internal forces, defining a stable failure trajectory. Subsequent increases in wind intensity accelerated progression along this predetermined path without activating alternative failure modes. This behavior validates the Markov formulation of irreversible, non-interchangeable damage states and underpins the probabilistic mapping of wind attack angles to distinct damage scenarios.

To record the mechanical degradation associated with each of these member-specific damage scenario, the Lemaitre strain equivalence hypothesis [47] was adopted. This approach simulates damage accumulation by reducing the elastic modulus of buckled members in proportion to their loss in stiffness while preserving the geometric integrity of the tower. For each identified damage scenario D_i, the calibrated modulus reductions yield a corresponding *"damage-recorded"* FEM (FEM-D). Although ten damage scenarios were identified, mirrored scenarios are structurally equivalent (cf. Fig. 5(a)), reducing the number of distinct FEM-Ds to six (i.e., $D_1 - D_6$), with transition probabilities for symmetric cases mapped from simulations in Section 3.3. These FEM-Ds serve as the physically grounded and computationally efficient basis for estimating the damage-to-collapse transition probability $p_{D_i \to C}$ in the CTPF framework.

To further determine the collapse threshold ls_C, each pushover analysis was carried well past the first buckling event—up to the point of global instability or numerical divergence (Fig. 5(a)). All pushover curves show a clear inflection marking global buckling, but this onset underestimates post-buckling capacity. Conversely, defining collapse at the curve's ultimate endpoint can be overly optimistic. By surveying

results across all attack angles, we therefore adopt a fixed-height-ratio criterion: ls_C = 2.5 % of tower height. This single threshold strikes a practical balance—capturing the loss of serviceability after significant deformation while accounting for residual capacity—yielding a consistent threshold of collapse for both intact state and every damage scenario.

Together, the intact FEM, the six distinct FEM-Ds, the damage thresholds $ls_{D_i}^{(\Theta)}$ and collapse threshold ls_C furnish a physically transparent foundation for the subsequent CTPF derivation, as summarized in Fig. 5(c).

3.3. Probabilistic nonlinear time-history analysis and derivation of CTPFs

While pushover analyses are effective for identifying damage and collapse thresholds and developing FEM-Ds, they do not capture the rapid fluctuations in wind speed and direction that occur in reality. These dynamic effects and spatial turbulence significantly influence the likelihood of structural damage or collapse. To model these stochastic phenomena, probabilistic nonlinear time-history simulations were conducted on the intact FEM and the FEM-Ds of the tower-line system. The outcomes of these simulations are a set of wind speed-dependent CTPFs that specify the likelihood of each state transition (e.g., $s_O \rightarrow s_{D_i}$, $s_{D_i} \rightarrow s_C$) at given attack angles, following the fragility-based formulation [21]. A total of 144 such functions were derived: 24 for intact towers (12 directions each for transitions to specified damage and collapse), and 120 for pre-damaged towers (12 directions for each of 10 damage states to collapse).

The derivation of CTPFs involves a four-step procedure:

1. **Generation of synthetic wind samples:** For each mean wind speed across a spectrum of wind intensities, generate an ensemble of stochastic time-history samples using the Davenport spectrum and linear filtering. These realizations reproduce realistic wind fluctuations for subsequent dynamic analysis.
2. **Dynamic response simulation:** Apply each synthetic wind time-histories to the tower-line FEM, both in its intact state (Section 3.1) and in each of the six distinct damage configurations (i.e., FEM-Ds) under varying wind attack angles. Record the tower-top displacement time series.
3. **Limit state mapping:** For each run, compare the peak displacement to the damage threshold ls_D and (or) the collapse threshold ls_C. Classify the outcome as “no transition”, “damage”, or “collapse”.
4. **Statistical analysis and fitting:** At each wind speed, compute the empirical frequency of each transition across the ensemble (e.g., $s_O \rightarrow s_{D_i}$, $s_O \rightarrow s_C$, and $s_{D_i} \rightarrow s_C$), and fit lognormal cumulative distribution function (CDF) for each attack angle to obtain CTPFs.

Fig. 6(a and b) illustrates a representative wind time history for a 27 m/s mean speed and its match to the target Davenport spectrum, confirming our synthetic-wind accuracy. At each time step t, the instantaneous wind load on tower segments $W_s(t)$ and the transverse wind loads on lines $W_x(t)$ are computed per the technical code:

$$W_s(t) = \frac{1}{2}\rho\mu_s A_s[u(t)]^2 \tag{21}$$

$$W_x(t) = \frac{1}{2}\rho\mu_{sc} dl \sin^2\Theta[u(t)]^2 \tag{22}$$

where $u(t)$ is the instantaneous wind speed (including both mean and fluctuation parts); Θ, the wind attack angle; ρ, air density; μ_s and μ_{sc}, shape coefficients of tower components and lines; A_s, the projected area of tower components normal to the wind; d, the outer diameter of the lines; and l, the line segment length (see Fig. 4(g) along with loading points).

For each wind attack angle Θ, the tower-top displacement is monitored and compared with the corresponding damage ($ls_{D_i}^{(\Theta)}$) and collapse (ls_C) thresholds in each time-history run. Starting from state s_O, the tower may remain elastic, trigger a damage state s_{D_i}, or proceed directly to collapse s_C. Likewise, simulations beginning in a damage state may either stay in that state or progress into collapse. Fig. 6(c and d) compares the intact and s_{D_1} models under the 27 m/s wind in Fig. 6(a) both at 0° wind attack angle: the intact tower exceeds its damage threshold but not collapse, whereas the pre-damaged tower exceeds both thresholds, illustrating its heightened fragility.

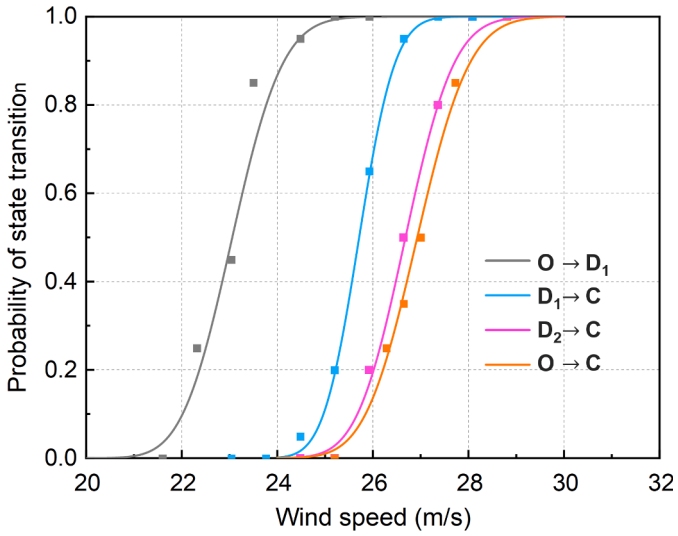

Fig. 7. Representative CTPFs for key state transitions under 0° wind attack.

The wind speed-dependent CTPFs, are constructed by counting, for each mean wind speed, the fraction of simulations in which a given transition occurs (e.g., $s_O \rightarrow s_{D_i}$, $s_O \rightarrow s_C$, or $s_{D_i} \rightarrow s_C$). These empirical probabilities are then fitted with lognormal CDF, yielding smooth, monotonic CTPFs that correspond to the exceedance probabilities defined in Eqs. (8–10). Leveraging load and structural symmetries, 76 independent CTPFs were directly fitted from simulations, with the remaining obtained via symmetry-based mapping across wind attack angles and damage configurations, substantially reducing computational cost.

To balance accuracy and efficiency, we calibrated our ensemble size by comparing CTPF fits using 20 versus 100 Monte Carlo simulations at the critical 0° attack angle. Increasing the sample count yielded changes in collapse probability estimates of less than 0.1 across the key wind-speed range (25–28 m/s), in line with prior studies (e.g., [10]). Thus, we employ 20 wind-realizations per state-intensity-direction combination. As discussed in Section 2, uncertainties in structural parameters are deemed secondary relative to wind-load fluctuations in the proposed framework and are therefore not explicitly modeled here, with material properties taken as standard values and geometric dimensions as mean values. Nonetheless, the framework is flexible and can readily accommodate such extensions by sampling key properties to generate structurally varied ensembles [33,48].

Fig. 7 shows example CTPFs for key transitions at 0° attack. Pre-damaged towers (e.g., s_{D_1}) collapse at substantially lower wind speeds than intact towers (s_O), and different damage scenarios yield different collapse probabilities—highlighting how the location and severity of pre-existing damage govern subsequent vulnerability. Finally, the analyses preserve the physically realistic ordering $p_{D_i \rightarrow C}(W_t) \geq p_{O \rightarrow C}(W_t)$; that is, the collapse probability from any damage state is always greater than—or at minimum equal to—that of an intact tower.

(a) Parameters of CTPFs and correspondence with the Markov process

State Transitions	Parameter	Wind Attack Angle 0°	30°	60°	90°	120°	150°	180°	210°	240°	270°	300°	330°
$O \rightarrow D_i$	μ (m/s)	23.1	24.5	35.3	46.6	35.1	24.2	22.5	24.2	35.1	46.6	35.3	24.5
	σ	0.036	0.03	0.068	0.079	0.069	0.029	0.032	0.029	0.069	0.079	0.068	0.03
$O \rightarrow C$	μ (m/s)	26.9	30.8	46.8	59.3	47.5	32.2	28.1	32.2	47.5	59.3	46.8	30.8
	σ	0.032	0.042	0.043	0.059	0.052	0.041	0.036	0.041	0.052	0.059	0.043	0.042
$D_1 \rightarrow C$	μ (m/s)	25.7	30.4	46.6	58.8	47.2	31.7	27.8	31.7	47.2	58.8	46.6	30.4
	σ	0.023	0.042	0.036	0.053	0.046	0.029	0.031	0.029	0.046	0.053	0.036	0.042
$D_2 \rightarrow C$	μ (m/s)	26.7	30.7	46.7	59.0	47.4	32.1	27.9	31.9	47.1	59.0	46.8	30.5
	σ	0.03	0.035	0.043	0.054	0.051	0.033	0.034	0.038	0.047	0.054	0.04	0.038
$D_3 \rightarrow C$	μ (m/s)	26.6	30.7	46.7	58.6	47.2	31.7	27.8	31.6	47.1	58.7	46.5	30.4
	σ	0.029	0.036	0.043	0.059	0.046	0.029	0.031	0.036	0.047	0.058	0.037	0.038
$D_4 \rightarrow C$	μ (m/s)	26.8	30.7	46.8	59.0	47.2	32.0	27.9	31.9	47.9	59.0	46.6	30.5
	σ	0.029	0.035	0.041	0.053	0.046	0.037	0.036	0.041	0.042	0.054	0.04	0.038
$D_5 \rightarrow C$	μ (m/s)	26.7	30.7	46.8	59.1	47.2	32.0	27.9	31.8	48.0	59.1	46.8	30.5
	σ	0.032	0.035	0.04	0.052	0.046	0.037	0.034	0.039	0.041	0.052	0.042	0.037
$D_6 \rightarrow C$	μ (m/s)	26.6	30.6	46.5	58.9	47.2	31.7	27.6	31.7	47.2	58.9	46.5	30.6
	σ	0.032	0.034	0.037	0.057	0.046	0.031	0.027	0.031	0.046	0.057	0.037	0.034
$D_7 \rightarrow C$	μ (m/s)	26.7	30.5	46.8	59.1	48.0	31.8	27.9	32.0	47.2	59.1	46.8	30.7
	σ	0.032	0.037	0.042	0.052	0.041	0.039	0.034	0.037	0.046	0.052	0.04	0.035
$D_8 \rightarrow C$	μ (m/s)	26.8	30.5	46.6	59.0	47.9	31.9	27.9	32.0	47.2	59.0	46.8	30.7
	σ	0.029	0.038	0.04	0.054	0.042	0.041	0.036	0.037	0.046	0.053	0.041	0.035
$D_9 \rightarrow C$	μ (m/s)	26.6	30.4	46.5	58.7	47.1	31.6	27.8	31.7	47.2	58.6	46.7	30.7
	σ	0.029	0.038	0.037	0.058	0.047	0.036	0.031	0.029	0.046	0.059	0.043	0.036
$D_{10} \rightarrow C$	μ (m/s)	26.7	30.5	46.8	59.0	47.1	31.9	27.9	32.1	47.4	59.0	46.7	30.7
	σ	0.03	0.038	0.04	0.054	0.047	0.038	0.034	0.033	0.051	0.054	0.043	0.035

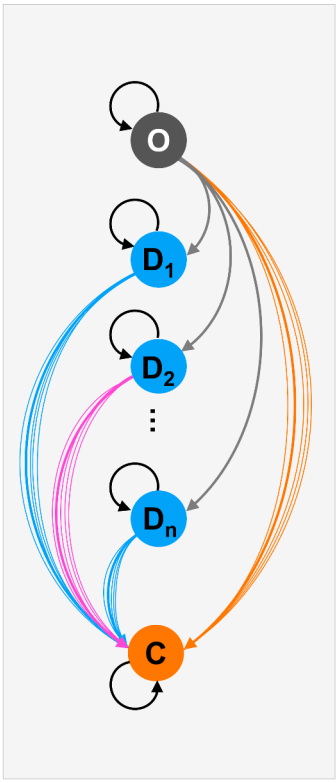

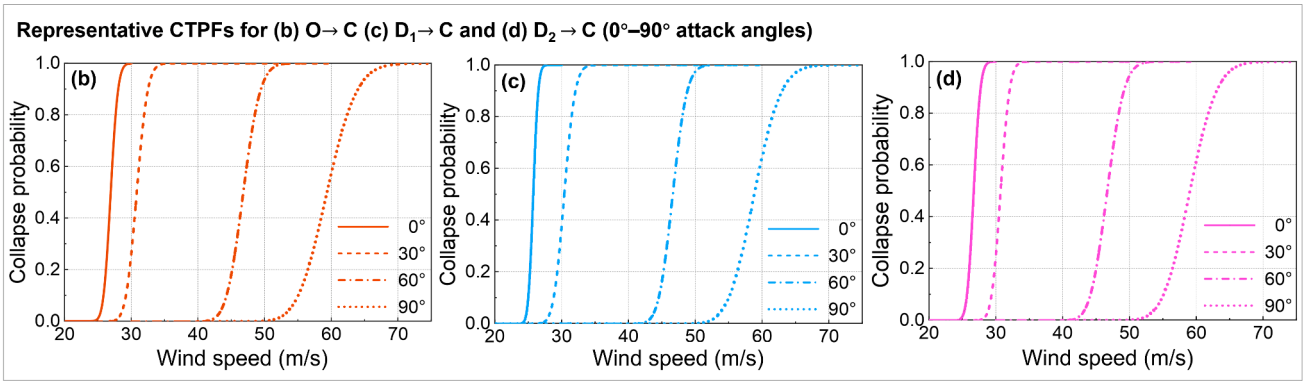

Fig. 8. (a) Parameters of CTPFs and correspondence with the Markov process; Representative CTPFs for state transition of (b) $O \rightarrow C$, (c) $D_1 \rightarrow C$, and (d) $D_2 \rightarrow C$ (0°–90° attack angles).

3.4. Assembly of the multi-state transition probability matrix

We tabulated the parameters of the 144 wind speed-dependent CTPFs, each fitted with a lognormal CDF. Specifically, the median wind speed μ and the shape parameter σ are reported in Fig. 8(a), with dashed-box values obtained through from symmetry mapping. Each row in the table represents a CTPF $p_{i \rightarrow j}$ as a function of the forecasted wind conditions $W_t = (V_t, \Theta_t)$. From the full CTPF library, several critical fragility trends can be identified:

(1) Fragility Hierarchy Across States

State transitions respect a clear ordering: *intact* → *damage* precedes *intact* → *collapse* and *damage* → *collapse*. For example, in Fig. 8(a) under a 0° wind attack, damage onset ($s_O \rightarrow s_{D_1}$) occurs at a median wind speed of ~23.1 m/s, whereas direct collapse ($s_O \rightarrow s_C$) initiates at ~26.9, and $s_{D_1} \rightarrow s_C$ reaching 50% probability occurs at just ~25.7 m/s. Once a tower enters a damage state, its remaining capacity plummets—demonstrating how pre-existing damage sharply raises collapse risk.

(2) Directional Vulnerabilities and Damage Severity

Wind attack angle profoundly shifts fragility. For example, the direct collapse median under 90° is roughly double that at 0°, owing to reduced conductor coupling. Off-axis attacks (e.g., 30°) can still trigger early damage onset (e.g., $s_O \rightarrow s_{D_2}$ at 24.5 m/s) even while collapse resistance remains relatively high. Comparing Fig. 8(c and d) shows that D_1-type damage (from 0° winds) cuts capacity far more than D_2-type damage (from 30° or 60° winds), illustrating that the location and mechanism of initial buckling dictate subsequent vulnerability.

(3) Amplified Sensitivity under Damage States

The shape parameter σ of CTPFs decreases once damage initiates, resulting in a narrower and steeper distribution. For instance, under 0° attack, the collapse probability for $s_{D_1} \rightarrow s_C$ jumps from 10% to 90%

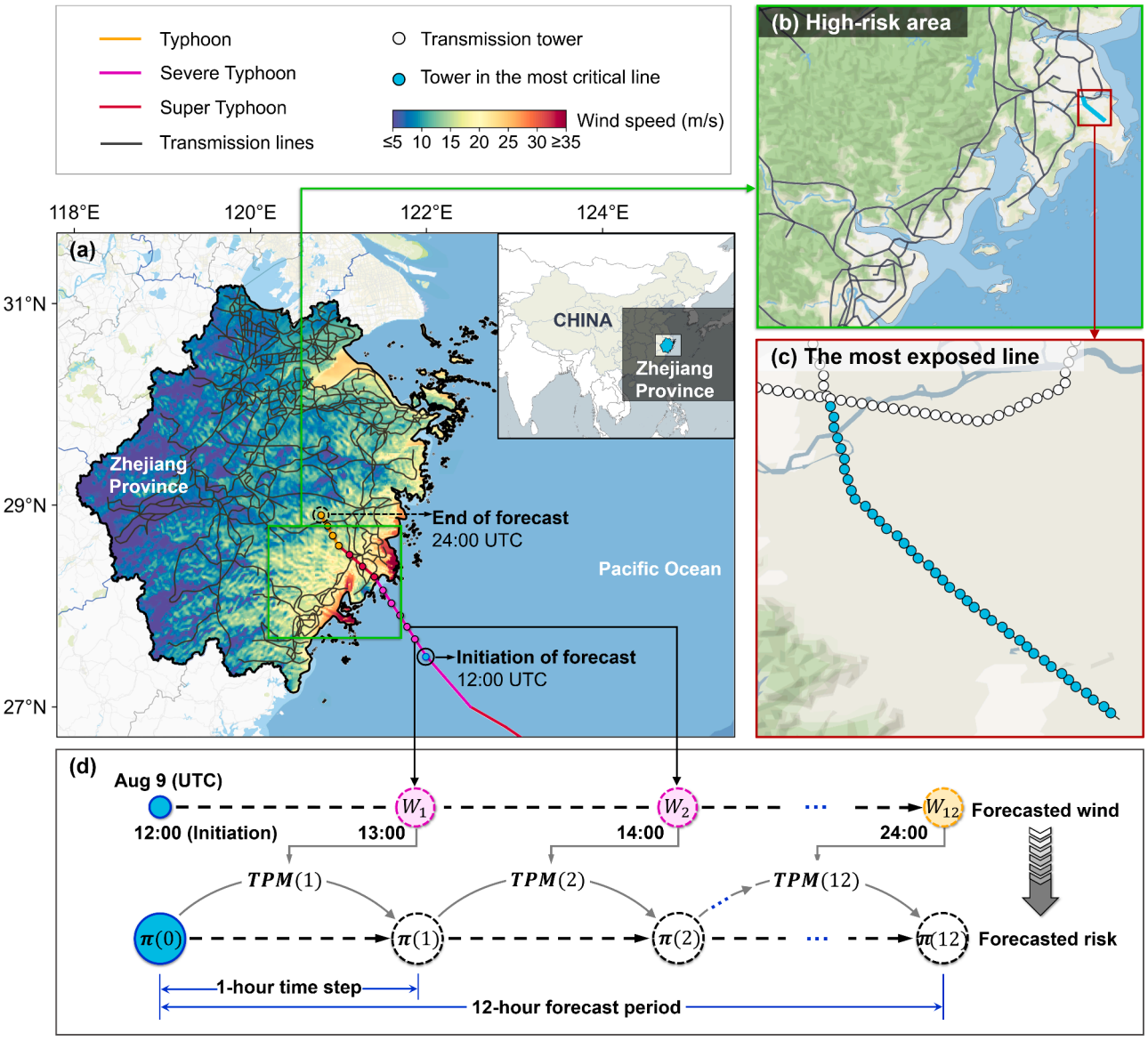

Fig. 9. (a) Forecasted wind field at Lekima's landfall and simplified transmission network in Zhejiang; (b) Zoomed-in high-risk area; (c) The most exposed transmission line; (d) MPRF using forecasted wind of Lekima.

within a 3 m/s window in Fig. 8(c), versus a broader 5 m/s window for $s_O \rightarrow s_C$ in Fig. 8(b). This steepening means that small wind speed increases after damage produce disproportionately large jumps in collapse risk, underscoring the urgency of early detection and intervention.

(4) Implications for Real-Time Forecasting

By capturing cumulative degradation, the CTPFs enable more accurate, time-evolving risk estimates. For instance, in Fig. 8(c), a tower in D_1 damage state at 0° that faces a subsequent 27 m/s gust is effectively certain to collapse, whereas treating it as intact would understate collapse probability at only 60% (cf. Fig. 8(b and c)). Such errors, when compounded over a multi-day TC event, could misdirect emergency response. The CTPFs therefore provide actionable thresholds (e.g., 23.1 m/s for $s_O \rightarrow s_{D_1}$) that grid operators can use for load routing, targeted inspections, or crew deployments—transforming static fragility data into dynamic, operations-ready risk forecasts.

Functioning as a repository of precomputed structural response, the CTPFs decouple intensive structural analyses from operational risk forecasting, enabling rapid real-time updates. With each new meteorological forecast, the ***TPM*** with pre-embedded CTPFs is dynamically populated to recursively propagate the tower's state vector and track capacity deterioration under sustained TC winds, based on which the failure and damage risks of towers and transmission lines—our primary concerns—can be quantified in step with evolving forecasts, as defined in Eqs. (16–19). Built upon CTPFs as its core engine, MPRF delivers granular, probabilistic insights into grid vulnerability, facilitating proactive resilience management during extreme wind events.

4. Application of MPRF framework during typhoon Lekima

Zhejiang Province, situated along the southeastern coast of China (Fig. 9(a)), is highly vulnerable to TCs, which pose severe risks to its critical power transmission infrastructure. These extreme wind events frequently result in the damage and collapse of transmission towers, leading to large-scale power outages and compromising the resilience of the regional power grid. Accordingly, real-time risk forecasting during TC events is essential for enhancing system resilience and supporting timely emergency response. To demonstrate the practical applicability of the proposed MPRF framework, a time-varying risk assessment is

Table 2
The number of towers in different ranges of $P_{C,t}^{tower}$ during the forecast period.

August 9 (UTC)	Risk category in terms of $P_{C,t}^{tower}$							
	(0.01,0.1] *Little Concern*		(0.1,0.5] *Watch List*		(0.5,0.9] *Potential Collapse*		(0.9,1] *Extreme Risk*	
	MPRF	BA	MPRF	BA	MPRF	BA	MPRF	BA
15:00	0	0	0	0	0	0	0	0
16:00	7	7	0	0	0	0	0	0
17:00	33	43	29	24	9	7	14	10
18:00	23	32	34	54	29	24	47	23
19:00	37	45	38	58	37	32	50	24
20:00	46	54	44	71	50	38	58	32
21:00	53	60	42	66	53	50	65	33
22:00	52	61	47	68	54	50	65	33
23:00	57	66	50	70	54	51	66	33
24:00	58	67	50	70	55	51	66	33

conducted for Super Typhoon Lekima of 2019.

4.1. Real-time risk forecasting of power transmission systems using MPRF in Zhejiang Province, China

For illustration, as in Fig. 9(a and d), the risk forecast—driven by forecasted wind speeds and directions as the primary model input—is conducted over a 12-hour window spanning Typhoon Lekima's landfall, with the initiation of the forecast at 12:00 UTC on August 9, 2019. This period captures the four hours leading up to and the eight hours following landfall (17:45 UTC on August 9, 2019). Given the complex hilly terrain that characterizes much of Zhejiang Province, the regional wind field is strongly influenced by microtopographic effects. To account for this complexity, the analysis is driven by high-resolution wind forecasts (443m × 443m grid) generated by Huang and Wang [29], from which tower-level inputs are extracted. As shown in Fig. 9(a), a snapshot of the downscaled wind field at the time of Lekima's landfall is overlaid with a sketch topology of the province's transmission system. The southeastern region of Zhejiang—which experienced the strongest winds during this period—is particularly vulnerable to typhoon-induced grid failures. A zoomed-in view of this high-risk area is presented in Fig. 9(b), which serves as the primary focus for the subsequent forecast illustration. Fig. 9(c) highlights the most exposed transmission line within this area.

At the start of the 12-hour window every tower is treated as intact, so the state vector is initialized as $\boldsymbol{\pi}(0) = (1, 0, \ldots, 0)^{\mathrm{T}}$. The transition-propagation rule in Eq. (5) is then applied recursively with the time-dependent $\boldsymbol{TPM}(t)$ to obtain $\boldsymbol{\pi}(t)$ for every subsequent hour, automatically accumulating any damage that occurs along the way. This process is illustrated in Fig. 9(d).

Two key considerations arise regarding its temporal and spatial implementation. Temporally, the assumed 1-hour increment reflects a balance between computational tractability and dynamic fidelity. While this resolution cannot fully capture sub-hourly gust-direction changes, such rapid directional shifts are generally less critical in tropical cyclones, where the large-scale vortex structure governs wind orientation relative to the storm center. The pressure gradient and storm track impose coherent, evolving wind fields, meaning that directional changes typically occur on timescales longer than one hour. Importantly, this 1-hour increment also aligns with the temporal resolution of available high-resolution meteorological forecast products, ensuring consistency between input data and model implementation. Spatially, for demonstration purposes, the same 2300ZM1-based CTPF library (Fig. 8(a)) is applied to all tower types in the study area. In an operational setting, however, each tower type would be characterized by its own CTPFs, ensuring that structural heterogeneity is fully represented and enabling finer granularity when scaling up to large transmission networks.

To highlight the benefit of modelling cumulative damage, we benchmark the tower-level forecasts from the MPRF against the widely used Binary Approach (BA) [21,10]. The BA treats every forecast step as an independent event: structural capacity is assumed to "reset," and the same intact-to-collapse fragility function $p_{O\to C}(t)$ is applied recursively as:

$$\pi_C(t) = \pi_C(t-1) + (1-\pi_C(t-1))\cdot p_{O\to C}(t) \tag{23}$$

Therefore, any damage that accumulated at time $t-1$ *cannot* weaken

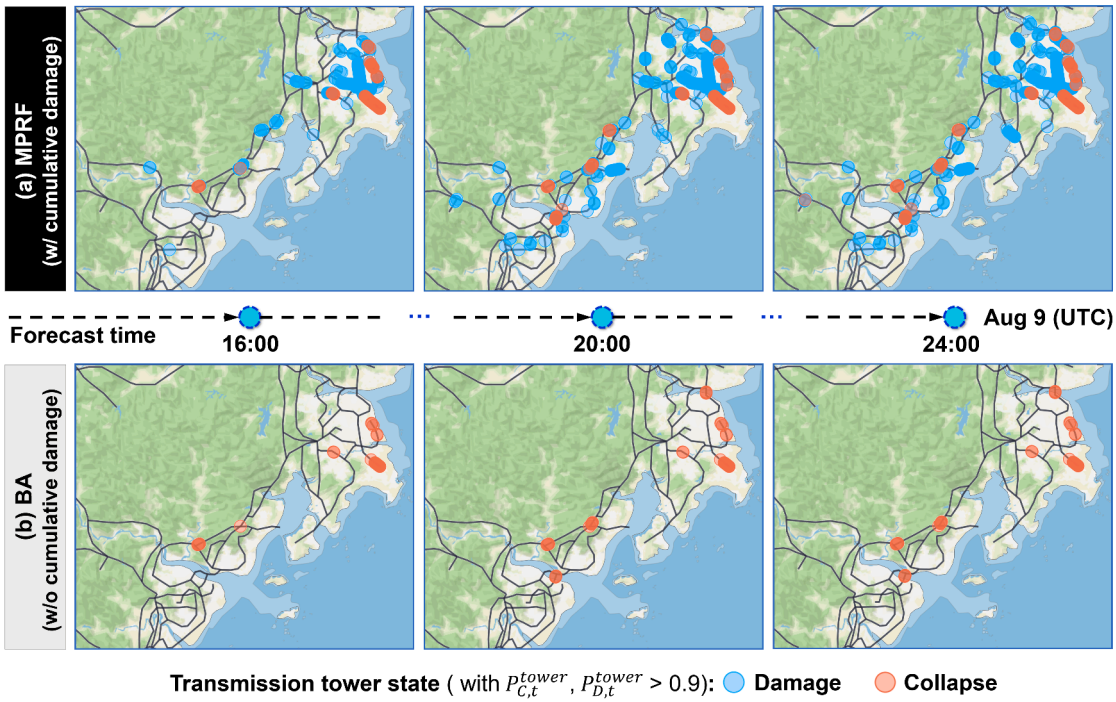

Fig. 10. High-risk towers ($P_{C,t}^{tower} > 0.9$ or $P_{D,t}^{tower} > 0.9$) forecasted by (a) MPRF and (b) BA at 16:00, 20:00, and 24:00 UTC, August 9.

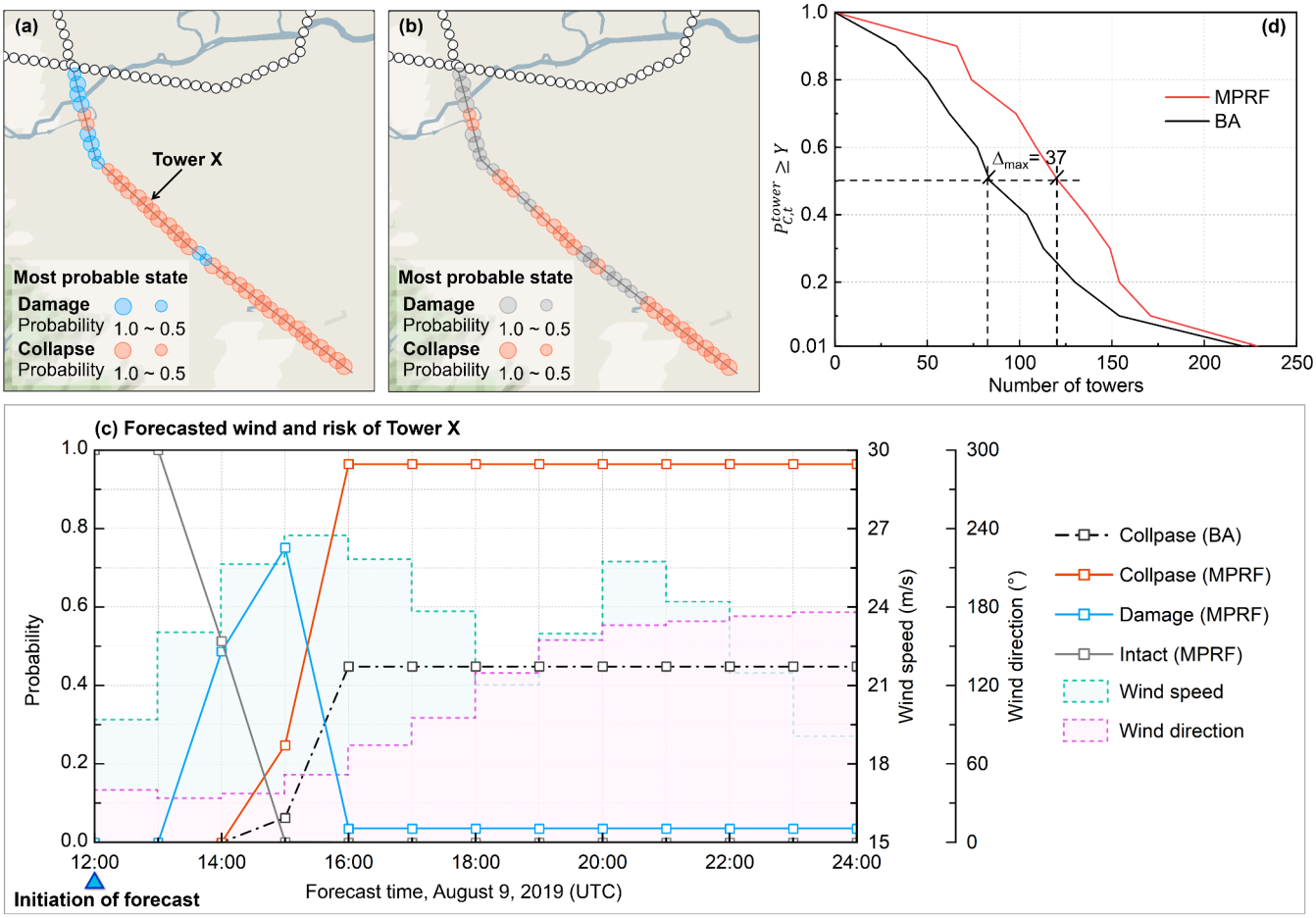

Fig. 11. Comparison of predicted tower states on the critical line at 24:00 UTC by (a) MPRF and (b) BA; (c) Forecast wind and risk of Tower X; (d) Tower exceedance counts at 24:00 UTC: MPRF vs. BA.

the tower at time t. By contrast, the MPRF updates the *full* state vector $\pi(t) = [\pi_O(t),\ \pi_{D_1}(t),\ \pi_{D_2}(t), \cdots,\ \pi_{D_{10}}(t),\ \pi_C(t)]^{\mathrm{T}}$ with the $\boldsymbol{TPM}(t)$, allowing damage incurred at one step to feed directly into the next. By combining Eqs. (16–19), cumulative failure and damage risks at the tower- and line-levels can be dynamically assessed.

4.2. Tower-level risk assessment

Table 2 summarizes the number of towers falling into four collapse-probability bands—*Little Concern* ($P_{C,t}^{tower} \leq 0.1$), *Watch List* (0.1–0.5), *Potential Collapse* (0.5–0.9), and *Extreme Risk* ($P_{C,t}^{tower} > 0.9$)—at each forecast hour. Around landfall (17:00–18:00 UTC) the MPRF places markedly more towers into the *Potential Collapse* and *Extreme Risk* bins than the BA. This gap opens because that winds at 17:00 are strong enough to *damage* many towers but not to collapse them outright, the MPRF "remembers" this incremental damage and consequently predicts a surge in collapse risk in subsequent time steps—a capability the memoryless BA cannot reproduce.

Fig. 10 shows that both the MPRF and BA identify at-risk towers in the high-risk area (Fig. 9(b)), confirming that local wind intensity governs collapse potential. However, the MPRF uniquely provide visibility of severe but standing towers (i.e., those with $P_{D,t}^{tower} > 0.9$), represented by blue dots in Fig. 10(a). The BA offers no equivalent metric, leaving operators blind to towers that are critically compromised yet not fully collapsed. Moreover, many towers tagged as "high damage" at earlier time steps evolve into "high collapse" in later forecasts, illustrating the sequential deterioration that the MPRF was designed to capture. For emergency response planning, such insights not only provide early warning, but also enables preemptive inspections and targeted interventions—crucial for preventing cascading failures and supporting more effective, time-sensitive decision-making.

We further compare the models along the most exposed transmission line in Fig. 9(c) at 24:00 UTC (Fig. 11(a–b)). MPRF predicts that virtually every tower on this corridor has either collapsed or entered a severely damage state, whereas BA still classifies many of the same structures as intact. This divergence mirrors field experience: typhoons rarely produce isolated collapses without leaving a trail of weakened towers that demand immediate attention. A representative Tower X marked in Fig. 11(a) demonstrates the contrast in Fig. 11(c). The wind record at this site shows sustained speeds above 20 m/s and wind directions sweeping through 0–180°, generating an exceptionally harsh load history. Although both models identify 16:00 UTC as the hour of collapse risk, MPRF start anticipates damage as early as 14:00 UTC. This damage accumulation leads MPRF to predict a maximum collapse probability of 96% by the time winds crest, while BA tops at 45%. Across the entire 12-h window, BA's neglect of damage accumulation yields systematic underprediction of collapse risk by up to 30%—an error large enough to mislead real-time operations.

The regional impact of that bias is summarized in Fig. 11(d): at the forecast's end, MPRF identifies 121 towers with $P_{C,t}^{tower} \geq 0.5$, 37 more than BA. Table 2 tracks the same divergence through time, showing that the gap opens soon after landfall and widens during the critical evening hours. Underestimating the number of high-risk towers can leave inspection crews under-deployed and mitigation actions delayed. These

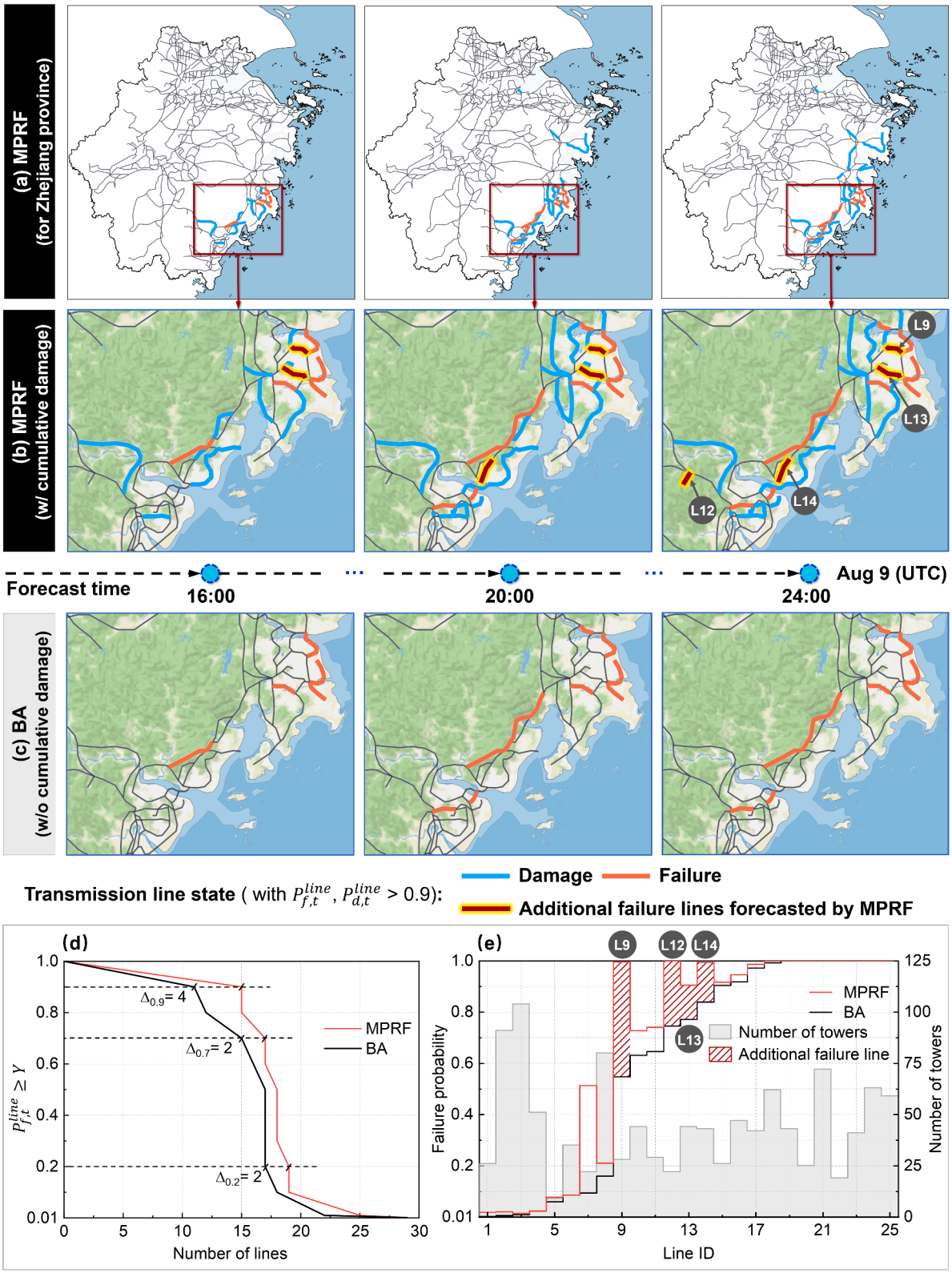

Fig. 12. (a) Spatial distribution of transmission lines with high collapse and damage risks ($P_{f,t}^{line}$, $P_{d,t}^{line}$ > 0.9) across Zhejiang Province predicted by MPRF at 16:00, 20:00, and 24:00 UTC; Line-scale comparison of collapse risks within high-risk area between (b) MPRF and (c) BA; Comparative analysis of (d) line exceedance counts and (e) failure probabilities: MPRF vs. BA at 24:00 UTC.

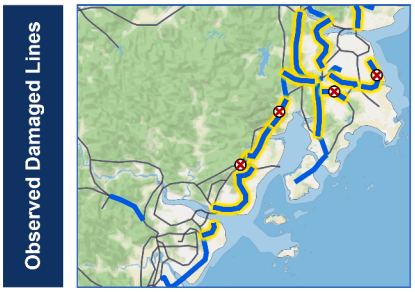

	Observed Damage	MPRF		BA
		Damage	Failure	Failure
Number of lines	28	9	5	4

Observed damaged lines
Observed damaged lines predicted by MPRF
Observed damaged lines predicted by BA

Fig. 13. Observed damaged lines and those predicted by MPRF ($P_{f,t}^{line}$ or $P_{d,t}^{line} > 0.9$) and BA ($P_{f,t}^{line} > 0.9$).

results underscore that operational risk forecast must account for damage accumulation—the mechanism embedded in the MPRF's Markov-based state propagation—if it is to provide grid operators with reliable, actionable intelligence during extreme-wind emergencies.

4.3. Line-level risk assessment

Fig. 12 shifts the focus from individual towers to entire transmission lines, revealing how cumulative damage modeling reshapes line-level risk profiles. In Fig. 12(a), MPRF flags 45 lines with either high collapse ($P_{f,t}^{line} > 0.9$) or damage ($P_{d,t}^{line} > 0.9$) risk by 24:00 UTC. Even lines with moderate collapse risk but high damage probabilities warrant targeted inspections and preemptive load management, since damage alone can compromise system integrity and accelerate future failures.

Fig. 12(b and c) further compare the line risk predictions of MPRF and BA in the high-risk area. BA can only label a line as "failed" or "non-failed", whereas MPRF distinguishes those that are structurally degraded but still standing (highlighted in blue), representing critical "warning" zones where damage may cascade into collapse if ignored. Moreover, MPRF consistently identifies more lines (darker red lines) at collapse risk. Fig. 12(d) tallies lines against escalating failure thresholds. At every thresholds—e.g., 0.2, 0.7, and 0.9—MPRF consistently predicts more high-risk lines than BA, highlighting that neglecting cumulative damage leads to under-forecasting of both imminent and emerging hazards. Finally, Fig. 12(e) quantifies how model divergence varies with line composition among the 25 transmission lines forecasted as being at risk of failure. Lines comprised of many lightly loaded towers show little difference between MPRF and BA—damage accumulation is diluted by the averaging across dozens of healthy towers. In contrast, lines whose risk is dominated by a handful of exposed towers preserve a sharp gap between the predictions of the two methods. Averaged over all lines, BA underestimates failure risk by roughly 28%, a systematic bias that can propagate into under-resourced emergency plans.

4.4. Validation with observational data

As an additional validation, post-event observational data on impacted transmission lines were obtained from State Grid Zhejiang Electric Power Co. and compared against predictions from MPRF and the benchmark BA model. As shown in Fig. 13, among the total 28 observed impacted lines, MPRF reproduces 14 (9 damaged and 5 failed), whereas BA captures only 4 failures. This demonstrates that by incorporating intermediate damage states, MPRF delivers markedly greater accuracy and captures a broader spectrum of system degradation, while BA's binary failure representation systematically underestimates impacts.

Some discrepancies between predictions and observations are expected, given the framework's reliance on wind field forecasts and the simplifications made for demonstration. While inherent uncertainties in microscale forecasts remain [29], future refinements—such as tower-specific CTPFs and assimilation of real-time meteorological or ensemble data—offer promising paths to further improve accuracy. Importantly, the framework consistently outperforms conventional BA approaches, providing both higher accuracy and richer representation of system degradation with 12-hour lead-time—an outcome that reinforces its practical utility and underscores its potential as a valuable tool for refining disaster loss estimations and guiding targeted interventions to strengthen grid resilience under evolving TC threats.

5. Conclusions and future work

This study introduced a Markov Process-based Risk Forecasting (MPRF) framework that advances real-time assessment of transmission towers subjected to tropical cyclone (TC) winds. The framework's central contribution is its explicit modeling of progressive, cumulative degradation: tower condition evolves through intact, direction-specific damage, and collapse states governed by time-varying winds. State evolution is implemented with a time-dependent transition probability matrix (TPM), populated from a library of conditional transition probability functions (CTPFs). Derived from high-fidelity pushover and nonlinear time-history simulations, these CTPFs shift the computational burden offline, providing a physically grounded yet tractable basis for probabilistic, time-evolving forecasting. Coupled with near real-time wind field inputs from meteorological forecasts or measurements, the pre-computed CTPFs render the MPRF framework broadly applicable in engineering practice. It enables temporally adaptive, spatially explicit, and multi-state risk forecast of transmission towers, offering an operationally scalable tool for proactive resilience planning and decision-making under evolving TC events.

The Typhoon Lekima (2019) case study highlighted MPRF's predictive power, showing it consistently identified high-risk towers earlier and with finer resolution than the benchmark BA model. By capturing progressive deterioration, it exposed vulnerabilities that BA overlooked, with BA's neglect of damage accumulation leading to collapse risks underestimated by nearly 30%%, a shortfall with serious implications for emergency response. Moreover, MPRF's forecasts aligned more closely with post-event records and provided richer diagnostic information, whereas BA's binary formulation systematically underrepresented system degradation. These results affirm MPRF's ability to generate risk forecasts that are not only more accurate than conventional approaches but also more faithful to observed impacts, reinforcing its role as a practical tool for strengthening grid resilience under intensifying TC hazards.

Despite its demonstrated strengths, several limitations highlight important directions for further development. The current line-level aggregation assumes independence among tower failures. While this ensures tractability and yields a conservative upper bound on line-level risk, it neglects spatial correlations from coherent wind fields and potential cascading effects along interconnected lines. In addition, the current formulation assumes monotonic deterioration, whereas in practice, towers may stabilize or recover capacity, either naturally or through repair interventions. To address this, the framework could be extended by dynamically adapting the TPM to include backward transitions or recovery states. These could be updated in real time through assimilation of inspection logs, UAV imagery, or SCADA reports.

Sequential Bayesian updating or particle filtering provide rigorous mechanisms to integrate such field data with forecasts, enabling the model to reconcile deterioration and intervention simultaneously. Similarly, although high-resolution meteorological forecasts were employed to drive grid risk forecast, accuracy inevitably depends on input quality. Real-time assimilation of weather-station observations, remote sensing, and ensemble forecasts would enhance robustness, particularly when data are sparse or uncertain during disaster. Beyond input quality, model validation remains constrained by the scarcity and confidentiality of post-disaster records. Broader access to observational data, expanded tower-specific CTPFs, and supplementary sources—such as sensing, inspection reports, or curated social media would enable more systematic evaluation. Addressing these limitations would sharpen MPRF's predictive power and support integration with outage, restoration, and socio-economic impact models. Such extensions would transform MPRF from a tower-level forecasting framework into a comprehensive decision-support platform for end-to-end resilience planning of power systems facing escalating TC hazards.

CRediT authorship contribution statement

Xinghong Chen: Writing – original draft, Visualization, Validation, Software, Methodology, Investigation, Formal analysis, Data curation, Conceptualization. **You Wu:** Software, Methodology. **Zhenguo Wang:** Data curation, Writing – review & editing. **Binbin Li:** Writing – review & editing, Methodology. **Naiyu Wang:** Writing – review & editing, Visualization, Supervision, Resources, Project administration, Methodology, Investigation, Funding acquisition, Formal analysis, Conceptualization, Validation.

Declaration of competing interest

The authors declare that they have no known competing financial interests or personal relationships that could have appeared to influence the work reported in this paper.

Acknowledgements

This research was supported by the State Grid Zhejiang Electric Power Co., Ltd. Science and Technology Research Project (Grant No. B311DS24001A). This support is gratefully acknowledged.

Data availability

Data will be made available on request.

References

[1] Darestani YM, Jeddi AB, Shafieezadeh A. Hurricane Fragility Assessment of Power Transmission Towers for a New Set of Performance-Based Limit States. In: Stewart MG, Rosowsky DV, editors. Engineering for Extremes, Springer Tracts in Civil Engineering. Cham: Springer International Publishing; 2022. p. 167–88. https://doi.org/10.1007/978-3-030-85018-0_8.

[2] Khodzhaiev M, Reuter U. Structural optimization of transmission towers using a novel Genetic Algorithm approach with a variable length genome. Eng. Struct. 2021;240:112306. https://doi.org/10.1016/j.engstruct.2021.112306.

[3] Mathakari S, Gardoni P, Agarwal P, Raich A, Haukaas T. Reliability-Based Optimal Design of Electrical Transmission Towers Using Multi-Objective Genetic Algorithms. Comput.-Aided Civil Infrastr. Eng. 2007;22:282–92. https://doi.org/10.1111/j.1467-8667.2007.00485.x.

[4] Cai Y, Wan J. Wind-Resistant Capacity Modeling for Electric Transmission Line Towers Using Kriging Surrogates and Its Application to Structural Fragility. Applied Sciences 2021;11:4714. https://doi.org/10.3390/app11114714.

[5] Zhang W, Xiao Y, Li C, Zheng Q, Tang Y. Wind load investigation of self-supported lattice transmission tower based on wind tunnel tests. Eng. Struct. 2022;252:113575. https://doi.org/10.1016/j.engstruct.2021.113575.

[6] Panteli M, Pickering C, Wilkinson S, Dawson R, Mancarella P. Power System Resilience to Extreme Weather: Fragility Modeling, Probabilistic Impact Assessment, and Adaptation Measures. IEEE Trans. Power Syst. 2017;32:3747–57. https://doi.org/10.1109/TPWRS.2016.2641463.

[7] Fu X, Li H-N, Li G. Fragility analysis and estimation of collapse status for transmission tower subjected to wind and rain loads. Structural Safety 2016;58:1–10. https://doi.org/10.1016/j.strusafe.2015.08.002.

[8] Fu X, Li H-N, Tian L, Wang J, Cheng H. Fragility Analysis of Transmission Line Subjected to Wind Loading. Journal of Performance of Constructed Facilities 2019;33:04019044. https://doi.org/10.1061/(ASCE)CF.1943-5509.0001311.

[9] Ma L, Khazaali M, Bocchini P. Component-based fragility analysis of transmission towers subjected to hurricane wind load. Eng. Struct. 2021;242:112586. https://doi.org/10.1016/j.engstruct.2021.112586.

[10] Xue J, Mohammadi F, Li X, Sahraei-Ardakani M, Ou G, Pu Z. Impact of transmission tower-line interaction to the bulk power system during hurricane. Reliab. Eng. Syst. Saf. 2020;203:107079. https://doi.org/10.1016/j.ress.2020.107079.

[11] Guo X, Li H, Zhang H. Damage risk assessment of transmission towers based on the combined probability spatial-temporal distribution of strong winds and earthquakes. Reliab. Eng. Syst. Saf. 2025;261:111078. https://doi.org/10.1016/j.ress.2025.111078.

[12] Bi W, Tian L, Li C, Ma Z. A Kriging-based probabilistic framework for multi-hazard performance assessment of transmission tower-line systems under coupled wind and rain loads. Reliab. Eng. Syst. Saf. 2023;240:109615. https://doi.org/10.1016/j.ress.2023.109615.

[13] Fu X, Li H-N, Li G, Dong Z-Q. Fragility analysis of a transmission tower under combined wind and rain loads. Journal of Wind Engineering and Industrial Aerodynamics 2020;199:104098. https://doi.org/10.1016/j.jweia.2020.104098.

[14] Tian L, Pan H, Ma R, Zhang L, Liu Z. Full-scale test and numerical failure analysis of a latticed steel tubular transmission tower. Eng. Struct. 2020;208:109919. https://doi.org/10.1016/j.engstruct.2019.109919.

[15] Asgarian B, Dadras Eslamlou S,E, Zaghi A, Mehr M. Progressive collapse analysis of power transmission towers. J. Constr. Steel. Res. 2016;123:31–40. https://doi.org/10.1016/j.jcsr.2016.04.021.

[16] Vettoretto G, Li Z, Affolter C. Evaluation of the Ultimate Collapse Load of a High-Voltage Transmission Tower under Excessive Wind Loads. Buildings 2023;13:513. https://doi.org/10.3390/buildings13020513.

[17] Raj, S.V., Kumar, M., Bhatia, U., 2021. Fragility curves for power transmission towers in Odisha, India, based on observed damage during 2019 Cyclone Fani. https://doi.org/10.48550/arXiv.2107.06072.

[18] Li J-X, Yang T, Zhang C, Sun L, Qu C-X. Typhoon fragility analysis of transmission tower-line system considering wind-induced fatigue. Eng. Struct. 2025;338:120572. https://doi.org/10.1016/j.engstruct.2025.120572.

[19] Zhang X, Xie Q. Cumulative damage risk assessment for transmission tower-line system considering copula-based joint distribution of wind speed and direction. Reliab. Eng. Syst. Saf. 2026;265:111595. https://doi.org/10.1016/j.ress.2025.111595.

[20] Zhang X, Xie Q, Li X, Wu H. Dynamic stability analysis of aging transmission tower-line system considering copula-based initial damage under wind loads. Thin-Walled Struct. 2025;214:113328. https://doi.org/10.1016/j.tws.2025.113328.

[21] Cai Y, Xie Q, Xue S, Hu L, Kareem A. Fragility modelling framework for transmission line towers under winds. Eng. Struct. 2019;191:686–97. https://doi.org/10.1016/j.engstruct.2019.04.096.

[22] Sang Y, Xue J, Sahraei-Ardakani M, Ou G. An Integrated Preventive Operation Framework for Power Systems During Hurricanes. IEEe Syst. J. 2020;14:3245–55. https://doi.org/10.1109/JSYST.2019.2947672.

[23] Mühlhofer E, Koks EE, Kropf CM, Sansavini G, Bresch DN. A generalized natural hazard risk modelling framework for infrastructure failure cascades. Reliab. Eng. Syst. Saf. 2023;234:109194. https://doi.org/10.1016/j.ress.2023.109194.

[24] Kim G, Kwag S, Eem S, Hahm D, Park JH. Probabilistic safety assessment of off-site power system under typhoon considering failure correlation between transmission towers. Reliab. Eng. Syst. Saf. 2025;254:110637. https://doi.org/10.1016/j.ress.2024.110637.

[25] Li Y, Ma L, Zhai C, Akiyama M, Qin H. A probabilistic framework for assessing and enhancing the resilience of power systems to typhoon hazards. Reliab. Eng. Syst. Saf. 2025;111607. https://doi.org/10.1016/j.ress.2025.111607.

[26] Ma L, Christou V, Bocchini P. Framework for probabilistic simulation of power transmission network performance under hurricanes. Reliab. Eng. Syst. Saf. 2022;217:108072. https://doi.org/10.1016/j.ress.2021.108072.

[27] Dikshit S, Dobson I, Alipour A. Cascading structural failures of towers in an electric power transmission line due to straight line winds. Reliab. Eng. Syst. Saf. 2024;250:110304. https://doi.org/10.1016/j.ress.2024.110304.

[28] Huang X, Wang N. Modeling probabilistic micro-scale wind field for risk forecasts of power transmission systems during tropical cyclones. Structural Safety 2025;116:102620. https://doi.org/10.1016/j.strusafe.2025.102620.

[29] Huang X, Wang N. An adaptive nested dynamic downscaling strategy of wind-field for real-time risk forecast of power transmission systems during tropical cyclones. Reliab. Eng. Syst. Saf. 2024;242:109731. https://doi.org/10.1016/j.ress.2023.109731.

[30] Wu Y, Wang N, Huang X, Wang Z. Enhancing power grid resilience during tropical cyclones: Deep learning-based real-time wind forecast corrections for dynamic risk prediction. Reliab. Eng. Syst. Saf. 2025;263:111284. https://doi.org/10.1016/j.ress.2025.111284.

[31] Du X, Hajjar JF. Methodology for collapse fragility development for hurricane events: Electrical transmission towers. J. Constr. Steel. Res. 2024;223:109005. https://doi.org/10.1016/j.jcsr.2024.109005.

[32] Du W-L, Fu X, Shao S, Li G, Li H-N, Yang F-L. Wind hazard reliability assessment of a transmission tower-line system incorporating progressive collapse. Reliab. Eng. Syst. Saf. 2025;257:110878. https://doi.org/10.1016/j.ress.2025.110878.

[33] Dikshit S, Alipour A. A moment-matching method for fragility analysis of transmission towers under straight line winds. Reliab. Eng. Syst. Saf. 2023;236:109241. https://doi.org/10.1016/j.ress.2023.109241.
[34] Bi W, Tian L, Li C, Ma Z, Pan H. Wind-induced failure analysis of a transmission tower-line system with long-term measured data and orientation effect. Reliab. Eng. Syst. Saf. 2023;229:108875. https://doi.org/10.1016/j.ress.2022.108875.
[35] Iannuzzi A, Spinelli P. Artificial Wind Generation and Structural Response. J. Struct. Eng. 1987;113:2382–98. https://doi.org/10.1061/(ASCE)0733-9445(1987)113:12(2382).
[36] Li J, Zhang C, Zhang J, Zhang X, Wang W. Failure Probability Analysis of the Transmission Line Considering Uncertainty Under Combined Ice and Wind Loads. Appl. Sci. 2024;14:10752. https://doi.org/10.3390/app142210752.
[37] ABAQUS/Standard Version 6.23 Analysis User's Manual. Dassault Systèmes Simulia Corp. USA: Rhode Island; 2023.
[38] Yun X, Gardner L. Stress-strain curves for hot-rolled steels. J. Constr. Steel. Res. 2017;133:36–46. https://doi.org/10.1016/j.jcsr.2017.01.024.
[39] Mara TG, Hong HP. Effect of wind direction on the response and capacity surface of a transmission tower. Eng. Struct. 2013;57:493–501. https://doi.org/10.1016/j.engstruct.2013.10.004.
[40] Zhang J, Xie Q. Failure analysis of transmission tower subjected to strong wind load. J. Constr. Steel. Res. 2019;160:271–9. https://doi.org/10.1016/j.jcsr.2019.05.041.
[41] Kong W, Zhu MW, Sheng ZL. The Find-Forming of Transmission Line in ANSYS. AMR 2011;328–330:939–42. https://doi.org/10.4028/www.scientific.net/AMR.328-330.939.
[42] Wang-Hai Z, Jian-Bin YU. Form-finding Analysis of Overhead Transmission Line based on ANSYS. Electric Power Construction 2012;33:32–5.
[43] McClure G, Lapointe M. Modeling the structural dynamic response of overhead transmission lines. Comput. Struct. 2003;81:825–34. https://doi.org/10.1016/S0045-7949(02)00472-8.
[44] GB50017-2017. Standard for design of steel structures. Beijing: China Architecture& Building Press; 2017. Chinese.
[45] Fu X, Li H-N. Uncertainty analysis of the strength capacity and failure path for a transmission tower under a wind load. Journal of Wind Engineering and Industrial Aerodynamics 2018;173:147–55. https://doi.org/10.1016/j.jweia.2017.12.009.
[46] DL/T5154-2002. Technology Regulation of Design for Tower and Pole Structures of Overhead Transmission Line. Chengdu, China: Southwest Electric Power Design Institute; 2002. Chinese.
[47] Lemaitre J. A Continuous Damage Mechanics Model for Ductile Fracture. J. Eng. Mater. Technol. 1985;107:83–9. https://doi.org/10.1115/1.3225775.
[48] Mohammadi Darestani Y, Shafieezadeh A, Cha K. Effect of modelling complexities on extreme wind hazard performance of steel lattice transmission towers. Structure and Infrastructure Engineering 2020;16:898–915. https://doi.org/10.1080/15732479.2019.1673783.